LAWRENCE
LIVERMORE
NATIONAL
LABORATORY

LLNL-JRNL-679716

Three-dimensional simulations of low foot and high foot implosion experiments on the National Ignition Facility

D. S. Clark

November 25, 2015

Physics of Plasmas

Disclaimer

Three-dimensional simulations of low foot and high foot implosion experiments on the National Ignition Facility

D. S. Clark, C. R. Weber, J. L. Milovich, J. D. Salmonson, A. L. Kritcher, S. W. Haan, B. A. Hammel, D. E. Hinkel, O. A. Hurricane, O. S. Jones, M. M. Marinak, P. K. Patel, H. F. Robey, S. M. Sepke, and M. J. Edwards
Lawrence Livermore National Laboratory, P.O. Box 808, Livermore, California 94550, USA

(Manuscript date January 29, 2016)

In order to achieve the several hundred Gbar stagnation pressures necessary for inertial confinement fusion ignition, implosion experiments on the National Ignition Facility (NIF) [E. I. Moses, R. N. Boyd, B. A. Remington, C. J. Keane, and R. Al-Ayat, Phys. Plasmas **16**, 041006 (2009)] require the compression of deuterium-tritium fuel layers by a convergence ratio as high as forty. Such high convergence implosions are subject to degradation by a range of perturbations, including the growth of small-scale defects due to hydrodynamic instabilities, as well as longer scale modulations due to radiation flux asymmetries in the enclosing hohlraum. Due to the broad range of scales involved, and also the genuinely three-dimensional (3-D) character of the flow, accurately modeling NIF implosions remains at the edge of current simulation capabilities. This paper describes the current state of progress of 3-D capsule-only simulations of NIF implosions aimed at accurately describing the performance of specific NIF experiments. Current simulations include the effects of hohlraum radiation asymmetries, capsule surface defects, the capsule support tent and fill tube, and use a grid resolution shown to be converged in companion two-dimensional simulations. The results of detailed simulations of low foot implosions from the National Ignition Campaign are contrasted against results for more recent high foot implosions. While the simulations suggest that low foot performance was dominated by ablation front instability growth, especially the defect seeded by the capsule support tent, high foot implosions appear to be dominated by hohlraum flux asymmetries, although the support tent still plays a significant role. For both implosion types, the simulations show reasonable, though not perfect, agreement with the data and suggest that a reliable predictive capability is developing to guide future implosions toward ignition.

I. INTRODUCTION

Various indirect drive inertial confinement fusion[1,2] ignition targets have now been tested at the National Ignition Facility (NIF)[3]. These include the low foot plastic ablator implosions tested during the National Ignition Campaign (NIC)[4], subsequent high foot implosions[5] also using plastic ablators, and more recently diamond[6] and beryllium[7] ablator implosions. While progress is being made in improving implosion performance, the ultimate goal of ignition has yet to be achieved and will require further innovation and improvements in implosion design.

To make progress in implosion design, however, requires a detailed understanding of the degradation sources present in current experiments. This, in turn, requires a close comparison of simulation results against the experimental data to verify that simulation models, and the failure modes they implicate, are in fact faithful representations of reality. Only once a standard simulation methodology has been thoroughly vetted against a range of implosion experiments can it be considered reliable for guiding future designs toward ignition. Moreover, a validated and reliable simulation model can also reveal details of the implosion dynamics and offer insights that may be impossible to extract directly from experimental data. For both of these reasons, detailed post-shot modeling, followed by a careful comparison of simulation results to the experimental data, is essential to progress in implosion design.

More specifically, in surveying the database of NIF experiments to-date, several questions arise, questions that are essential to answer in finding a path to improved performance. First, why did the NIC implosions perform as they did, that is, so far below pre-shot expectations? In particular, why did a handful of NIC shots appear to "mix" very heavily with up to 1 μg of ablator material believed to have entered the hot spot? Why did the high foot implosion series perform so much better in terms of yield (albeit at reduced compression), and can the same model explain this difference? Following several substantial advances in yield, why did the yield from high foot implosions appear to plateau? And finally, assuming simulations can reasonably reproduce the experimental trends for both implosion types, what design modifications are most likely to enable further performance gains?

To shed light on these questions, this paper describes progress in validating a post-shot simulation model of NIF implosion experiments using the radiation hydrodynamics code HYDRA[8]. These post-shot capsule-only simulations

aim to include everything that is know about a particularly implosion, in as much detail as possible given current computing capabilities, and hence to give the most complete simulation predictions that a detailed comparison with the experimental data requires. Current simulations include the effects of plastic (CH) ablator and deuterium-tritium (DT) ice surface roughness, radiation flux asymmetries from the surrounding hohlraum, surrogate models for the very fine-scale features such as the capsule support tent[9,10] and fill tube[11], and are run in realistic three-dimensional (3-D) geometry with a grid resolution that can be shown to be converged in companion two-dimensional (2-D) simulations. Surrogate perturbations must currently be used for the fill tube and tent since resolving those micron- and nanometer-scale features, respectively, requires hundreds of millions of simulation zones in 2-D and is therefore untenable for 3-D simulations on current computers. Nevertheless, current 3-D simulations resolve ~50 μm wavelength features (Legendre modes up to $\ell = 100$) over the full 4π solid angle of the capsule and hence capture the genuinely 3-D character of high-convergence NIF implosions in the presence of realistic perturbation sources. Of course, these simulations are computationally expensive and require ~400 million computational zones and roughly one month to complete on six thousand processors. As shown below, however, only fully 3-D simulations are capable of adequately reproducing the experimental results for the highest compression NIF implosions.

The results described below extend the work of Refs. 12 and 13 by updating low foot simulations to include the current best understanding of the perturbation sources present in NIC implosions (the impact of the tent and hohlraum radiation flux asymmetries in particular) and also to compare two low foot implosions: one with little evidence of ablator contamination in the hot spot[14,15] (a "clean" implosion) and one that showed evidence of significant ablator material entering the hot spot (a heavily "mixed" implosion). Additionally, 3-D post-shot simulations have now been completed for two high foot implosions. The high foot implosion design[16] derived from simulation studies during the NIC[17] showing that implosions driven with a higher radiation temperature during the early phase of the implosion (the "foot") are significantly more stable to ablation front Richtmyer-Meshkov[18,19] and Rayleigh-Taylor[20,21] instabilities. This improved stability, however, comes at the cost of reduced overall compression, and in this sense high foot implosions enter a different region in implosion parameter space. Simulating low foot and high foot experiments hence offers an opportunity to test modeling capabilities by challenging them to reproduce results for these quite different implosion types.

High foot simulation results have recently been reported in Ref. 22. These results are based on integrated hohlraum modeling[23] of the entire suite of high foot implosion experiments. Compared to the capsule-only simulations described here, integrated hohlraum simulations model the laser propagation through the hohlraum and its deposition and conversion to x-rays on the hohlraum wall, as well as the subsequent capsule implosion. This is advantageous in more comprehensively modeling the evolution of the experiment; however, it comes at the cost of reduced numerical resolution of the finer-scale dynamics of the capsule. In particular, these simulations ignore the impact of the capsule support tent. As shown recently[13,9], the tent was a significant degradation source for low foot implosions and likely also plays a role in high foot implosions. More importantly, the effective laser cone fraction is "tuned" empirically in these hohlraum simulations to match the experimental x-ray self-emission shape from the hot spot at bang time. Given that the presence of the tent perturbation is known to change the apparent hot spot x-ray shape in simulations, it can be expected that tuning the simulated hot spot shape to match the experiment, while ignoring the effect of the tent, results in an incorrect flux asymmetry being imposed in these simulations.

These hohlraum simulations also assume 2-D axisymmetry. While this may be an adequate approximation for sufficiently well behaved implosions, strongly perturbed implosions will certainly deviate from the 2-D idealization, and 2-D results should be compared to 3-D simulations to confirm whether or not the axisymmetric approximation is accurate. In particular, Ref. 22 reports that 2-D hohlraum simulations reproduce the observed high foot yields for implosion velocities less than ~350 km/s but over-predict the yields by as much as an order of magnitude at higher velocities. Burn-averaged ion temperatures are also under-predicted in simulations for higher velocity implosions, while neutron down scatter ratios (DSR, a measure of the overall compression of the implosion)[24] are over-predicted in simulations. An obvious question, then, is whether these discrepancies between simulation and experiment will be resolved if the effects of the tent and realistic 3-D geometry are properly included.

Given the significantly greater expense of running 3-D simulations compared to 2-D, only a few shots can be simulated in detail. The four shots chosen for this study are N120321, N120405, N130927, and N140819. These four shots are pictured in Fig. 1 in the plane of DT neutron yield versus fuel compression or ρR, along with other representative NIF implosions. Details of theses four shots are also summarized in Table I. Here the simulated adiabat is computed by mass averaging over the entire fuel (DT gas and ice) at the time of peak implosion velocity, and the convergence ratio is defined as the ratio of the initial outer capsule radius to the hot spot radius at bang time in a 1-D no-burn simulation. Of course, the adiabats are higher and the convergence ratios lower for the high foot suggesting that these implosions should be more stable. This stability is offset, however, by the higher velocities achieved with the higher laser powers used in these implosions.

NIF shot N120321 is significant since it is the highest

compression DT implosion yet fired on NIF. For this reason, it was analyzed closely in Ref. 13. Since that study was completed, however, detailed simulations of the impact of the capsule support tent[25] suggested that the tent acts as an even larger perturbation source than was assumed in those simulations. Further hohlraum modeling, aimed at better reproducing the results of 2-D convergent ablator (ConA) experiments[26], also refined the understanding of the flux asymmetries present in low foot hohlraums. Finally, the inferred hot spot mix mass has been revised downward for this shot based on more recent NIF data. Given these changes, the 3-D simulation of N120321 was rerun with updated inputs and is described as part of this study.

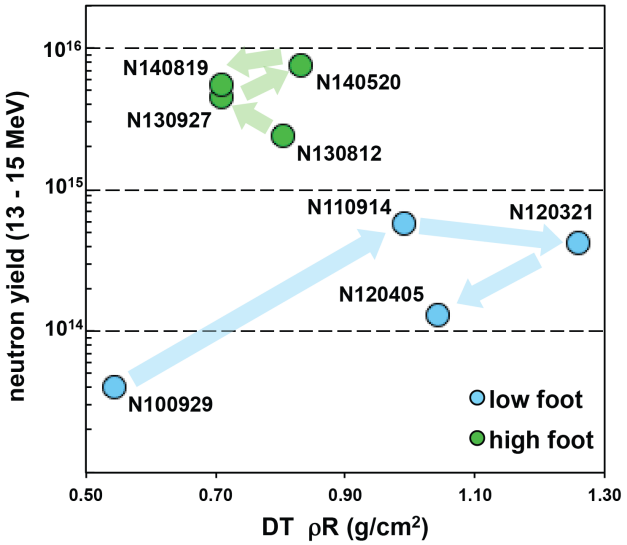

FIG. 1. (Color online) Summary of progress of NIC implosions and subsequent high foot implosions in the plane of DT neutron yield versus fuel areal density. The blue symbols represent low foot shots from the NIC, and the green symbols represent high foot shots. The arrows show the progression of each campaign over time. N120321 reached the highest compression of any DT shot yet fired on NIF, yet its higher power companion N120405 performed much worse. The high foot shot N130927 was the first NIF implosion to demonstrate "fuel gain" and was followed by higher power, thinner shell implosions that approached neutron yields of 1.0×10^{16}. The thinnest shell, highest power high foot N140819, however, appeared to go over a "cliff" and showed a drop in performance.

An important companion shot to N120321 was shot N120405. After N120321 demonstrated the highest compression yet achieved in a NIF implosion, N120405 raised the laser power and energy from 320 TW/1.5 MJ to 370 TW/1.6 MJ with the aim of increasing the implosion velocity and neutron yield at the same high compression demonstrated with N120321. As illustrated in Fig. 1, however, the yield and compression both dropped for N120405, as did the burn-averaged ion temperature. Subsequent analysis also suggested that up to 750 ng of ablator material mixed into the hot spot on N120405 while only 0–75 ng of mix were inferred for N120321. Evidently, a "cliff" in performance was crossed in going from N120321 to N120405, and understanding the physics of this cliff makes this pair of shots particularly important to study.

TABLE I. NIF experiments simulated in this study.

	low foot		high foot	
	N120321	N120405	N130927	N140819
shell thick. (μm)	194.9	194.7	195.0	164.8
tent thick. (nm)	110	110	45	45
E_{laser} (MJ)	1.5	1.6	1.8	1.8
P_{laser} (TW)	320	370	380	390
sim. vel. (km/s)	319	332	353	390
sim. adiabat	1.6	1.4	2.7	2.7
sim. conv. ratio	45	41	37	36
hot spot mix (ng)	0 – 75	500 – 725	0 – 150	0 – 150
T_{ion} (keV)	3.1	1.7	4.4	5.5
DSR (%)	6.2	5.1	3.5	3.5
$Y_{13-15\,MeV}$	4.2×10^{14}	1.3×10^{14}	4.4×10^{15}	5.5×10^{15}

In a different region of the yield versus ρR plane in Fig. 1 are the high foot implosion experiments. While these implosions reached roughly half the compression of the low foot, they did reach neutron yields up to an order of magnitude higher. Clearly, this represents a different region of implosion parameter space and raises the question of whether the same simulation methodology can model both the high compression, low foot implosions as well as the lower compression, but higher yield high foot implosions. As a test of the same methodology used to model N120321 and N120405, the high foot shot N130927 was simulated. N130927 was a 380 TW/1.8 MJ implosion distinguished by being the first NIF implosion to demonstrate "fuel gain," that is, a neutron yield greater than the estimated peak fuel kinetic energy (~12 kJ). Note that this implosion is also simulated to have a noticably higher implosion velocity (353 km/s) than the two low foot implosions (319 and 332 km/s, respectively), and, like all high foot implosions, there is no evidence of ablator mix into the hot spot.

After N130927, subsequent high foot implosions tested higher laser powers and energies, and also investigated thinning the ablator by first 20 and then 30 μm[27]. As shown by the green arrows in Fig. 1, both of these changes initially resulted in improved performance up until the highest power, thinnest shell experiment N140819. Similar to the low foot companions N120321 and N120405, N140819 appears to have crossed a performance cliff relative to other high foot implosions and suffered a drop in neutron yield. Unlike N120405, however, there is no evidence of hot spot mix for this shot, and the challenge to post-shot modeling is to explain why the performance dropped. A tantalizing possible explanation is that, at shot time, N140819 was observed to have a pronounced sag in the capsule shell near the fill tube location. This sag is believed to have been caused by melting of the capsule shell under the ultraviolet irradiation used to cure the glue attaching the fill tube to the capsule. In the presence of the tent and fill tube, this sag would have produced an inherently 3-D perturbation that could have ruptured the shell and resulted in the observed, degraded performance. If this explanation proves correct, then the yield degradation seen with N140819 represents more of an accident than the result of some more

fundamental trend. If the yield degradation of N140819 is not accidental but the result of some more fundamental cause, however, identifying this effect is clearly crucial to any effort to further improve high foot performance. A 3-D simulation of N140819 is hence particularly important.

The essential results of this study are the following. For both the two low foot and two high foot implosions, the simulations roughly agree with the measured performance in terms of neutron yield, burn-averaged ion temperature, DSR, hot spot size (as measured by x-ray and neutron imaging), bang time, and burn width. However, not all observables are matched within the error bars and not all are matched equally well for all shots. In particular, for both high foot implosions, the simulations under-predict the ion temperature compared to the data. Interestingly, the 3-D high foot simulations also somewhat under-predict the neutron yield. Additionally, the high foot simulations tend to over-predict the DSR or compression in the implosions. At this time, it is impossible to distinguish whether these discrepancies result simply from incomplete knowledge of initial and boundary conditions or point to a more fundamental discrepancy in the underlying physical models used in the simulations. Higher resolution 2-D simulations meant to assess whether finer-scale mixing could contribute to DSR discrepancies suggest that this effect does not play a role.

This paper is organized as follows. Sec. II describes the 3-D simulation results for the two low foot implosions. Sec. III then describes the results for the two high foot implosions. Higher resolution 2-D simulations of all four implosions are described in Sec. IV. Sec. V summarizes and discusses implications for future experiments.

II. LOW FOOT SIMULATIONS

The post-shot simulations described here were run in a manner similar to that followed in Refs. 12 and 13. In order to maximize numerical resolution and fidelity in modeling the implosion, only the capsule is included in these simulations and the hohlraum is treated as a spherical boundary condition that is a source of x-ray flux. The x-ray flux applied to the capsule is adjusted iteratively in one-dimensional (1-D) simulations to match measured implosions characteristics taken from "keyhole" shock timing experiments[28], 1-D ConA implosion velocity measurements[29], and bang time measurements (time of peak neutron production). The spectral content of the x-ray flux is also adjusted to be consistent with ViewFactor measurements[30]. 2-D and 3-D hohlraum flux asymmetries are included from companion hohlraum simulations, and surface roughness perturbations are included based on pre-shot surface characterization including Phase-Shifting Diffraction Interferometry[31] and Atomic Force Microscopy[32] of the outer ablator surface as well as optical characterization of the DT ice layer at shot time[33]. While all shots simulated in this study used their individual surface roughness data, note that none was uniquely more or less rough than any of its companions. Finally, note that measurements using the Hydrodynamic Growth Radiography (HGR) platform[34,35,36] have so far largely validated the modeling of ablation front instability growth in both low foot and high foot implosions. The results of the 3-D simulations below can hence be expected to give a fairly reliable picture of acceleration phase instability development in these implosions.

As already noted, the very fine scale features such as the support tent and fill tube cannot be resolved when simulating the full angular extent of the capsule in 3-D, and surrogate models must currently be used. For the support tent, a linear growth factor analysis is applied to a 2-D simulation that fully resolves the 45 – 110 nm tent thickness[25], and a surrogate surface perturbation is derived that reproduces the fully resolved result but on a much coarser numerical grid. Note that previous simulations[13] used a surrogate perturbation tuned to reproduce observed inflight radiography signatures[9]. This surrogate perturbation was a simple cosine-shaped groove encircling the poles of the capsule with a width of 350 μm and a depth of 200 nm. The updated surrogate perturbation derived from growth factor analysis is an S-shaped perturbation with a peak-to-valley amplitude of 150 nm for the low foot and a width of approximately 600 μm. This surrogate perturbation also approximately reproduces the radiographic signatures but results in spikes penetrating the hot spot at bang time that are three to four times the amplitude of those with the previous perturbation. Note that, for the high foot implosions discussed below, a similar S-shaped perturbation, also derived from growth factors, is used, but in this case the amplitude is 220 nm with the width unchanged. Interestingly, even though the initial tent thickness is smaller for the high foot implosions (45 versus 110 nm), detailed simulations suggest that the effective perturbation seeded with the high foot pulse shape is actually larger than with the low foot. The much reduced ablation front growth factors with the high foot, however, offset this larger initial perturbation such that the final perturbation from the tent is substantially reduced, as shown below. Finally, for the fill tube, a simple Gaussian divot perturbation is added to the ablator surface, and the depth and width of the perturbation adjusted to match the jetting behavior found in fully resolved 2-D fill tube simulations.

Fig. 2 shows the implosion sequence from the updated 3-D simulation of N120321. The outer surface in each rendering shows the ablation front defined as $1/e\times$ the maximum 1-D density at that time and is colored by the electron temperature. The two cutaways show the ion temperature (left) and density (right). Note that the temperature color scales are static, but the density color scale and the spacial scale change to follow the progression of the implosion in time. The hohlraum axis is vertical, and the time sequence progresses from left to right and top to

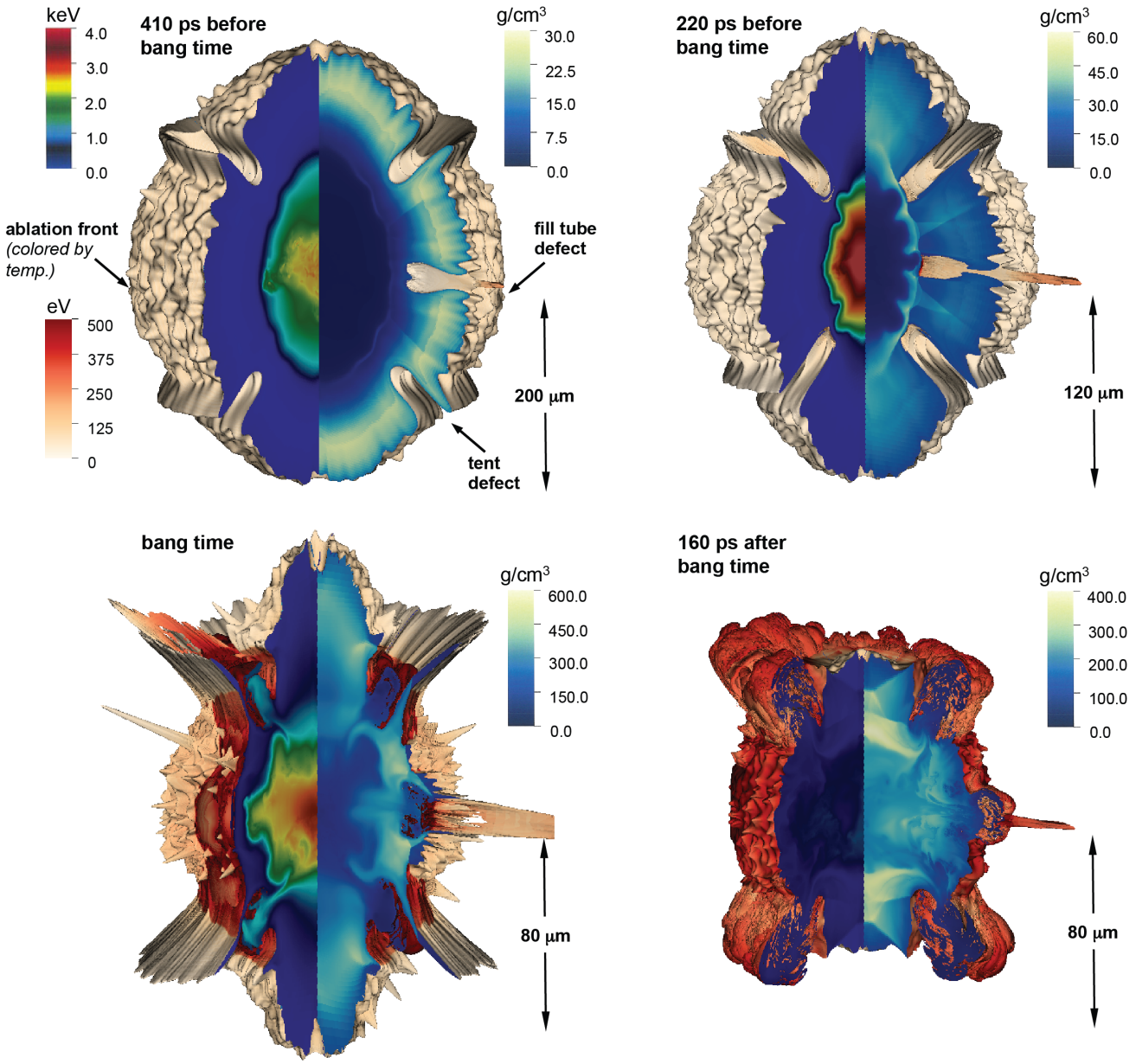

FIG. 2. (Color online) Stagnation sequence from the 3-D simulation of N120321 showing times from just before peak implosion velocity (410 ps before bang time) to the end of the simulation (160 ps after bang time). In each rendering, the outer surface shows the ablation front as defined by $1/e\times$ the maximum density at that time and is colored by the electron temperature with the color scale on the lower left. The left half of each cutaway shows the ion temperature with the color scale on the upper left, and the right half of each cutaway shows the density with the color scale on the right. The temperature color scales are fixed in time, but the density color scale, and the spatial scale, change to follow the implosion in time. The dominating effect of the tent is evident at each time.

bottom from shortly before the time of peak implosion velocity to the final time of the simulation when the burn rate has dropped to 1% of its maximum.

The growth of the various perturbation sources in the implosion is readily apparent. The large grooves encircling the north and south poles result from the tent perturbation, while the fill tube defect can be seen penetrating from the right side in this view. Random modulations are also growing on the ablation front seeded by surface roughness. As time progresses, the depth of the tent defect grows to nearly penetrate the shell, and fingers of cold, dense DT begin to fall into the hot spot due to deceleration phase Rayleight-Taylor growth. The increasingly prolate shape of the implosion due to the hohlraum flux asymmetries is also apparent. At bang time, the tent perturbation has caused two gashes to penetrate the shell around the north and south poles. These tent gashes clip off both ends of the otherwise prolate hot spot and reduce the hot spot volume to roughly a

third of what results without the tent perturbation present.

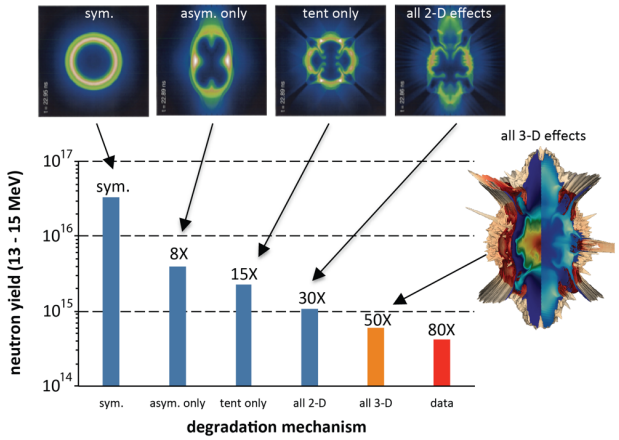

FIG. 3. (Color online) Relative impact of each perturbation source on neutron yield from 2-D simulations of N120321, as well as the 3-D simulation and experimental yields. The insets show the density distributions from 2-D simulations at bang time and the 3-D simulation result. The tent is the largest single source of yield degradation followed by the hohlraum flux asymmetries and surface roughness (not shown). In combination, all 2-D effects result in a factor of thirty reduction in yield from 1-D. All 3-D effects result in a factor of fifty yield reduction and bring the simulation results to just above the measured yield.

These gashes also weaken the shell and open an avenue for the high pressure hot spot to vent. In the last frame of the figure, this venting can be seen in the four-fold pattern of the hot spot blowing out through the weak spots caused by the combined effects of the tent and the low-mode flux asymmetries.

To assess the relative importance of the individual perturbation sources in this implosion, Fig. 3 compares the results in the form of neutron yield from 2-D simulations with each source added individually. The collective result of all 2-D perturbation sources and the 3-D result just described are also shown. For this implosion, the symmetric, unperturbed yield is simulated to be 3.3×10^{16}. Including the 2-D hohlraum asymmetries only results in a ~8× reduction in yield to 3.9×10^{15}. The tent perturbation alone results in a 15× yield reduction to 2.2×10^{15}. Surface roughness alone (not shown) results in a 5× reduction in yield. As can be seen from the insets, while the flux asymmetries strongly distort the hot spot into a highly prolate shape, they do not result in cold material deeply penetrating the hot spot. The tent perturbation on the other hand injects fingers of cold DT deep into the hot spot resulting in nearly twice the yield degradation. Based on these results, the tent was evidently the dominant perturbation for N120321. All 2-D perturbations in combination result in a 30× yield degradation to 1.1×10^{15}, and finally the 3-D simulation results in a 50× yield degradation to 6.0×10^{14}. This is close to but still slightly higher than the experimental yield of 4.2×10^{14}. Note that there is almost a factor of two degradation in yield between 2-D and 3-D simulations for this highly perturbed implosion.

Fig. 4 shows the analogous implosion sequence as Fig. 2 but for the higher power low foot shot N120405. The characteristics of the implosion sequence for N120405 are broadly similar to those of N120321. With the increased acceleration and convergence of this higher power implosion, however, the growth of perturbations at the ablation front is magnified. The defect caused by the tent perturbation has grown even larger than in N120321 and the random surface defects have grown into larger radiating spikes. In this case, the tent defect cuts cleanly through the north and south poles of the imploding shell roughly 150 ps before bang time and not only clipped both ends of the hot spot, as in N120321, but, by bang time, ejected the hot spot from the center of the implosion off to one side. As a consequence, whereas the simulation of N120321 maintained a small pocket of low density DT with a temperature of ~3 keV, the N120405 simulation barely reaches a central temperature of 1.5 keV.

More importantly, focusing on the bang time frame in Fig. 4, many small modulations can be seen in the density cutaway in the neighborhood of the tent defect. These are small globules of ablator material that have been entrained by the tent defect, drawn into the center of the hot spot, and stirred throughout the hot spot by the highly chaotic flow there. Post-processing this simulation shows that ~500 ng of ablator material has mixed into the inner 30 μm by bang time. This value is in agreement with what is inferred experimentally for this shot and appears to explain the origin of the hot spot mix mass inferred for N120405 as compared to N120321. That is, the amplification of the tent defect that occurred with the higher ablation front growth in N120405 pushed this perturbation source over the "cliff" of allowing a large amount of ablator material to enter the hot spot. Note that only such a large defect area as the tent that encircles the entire capsule azimuth appears to be capable of introducing as much mix mass as was observed on this shot. Simulations of localized surface defects or dust grains that occupy a small solid angle appear to be simply inadequate to explain the large mass injection. Note also that 2-D simulations that fully resolve the tent defect[25] show a similar amount of entrained ablator mass entering the hot spot but, due to the enforced axisymmetry of 2-D, the ablator material remains encased in a finger of DT fuel and is not mix through the hot spot as the 3-D simulation allows. 3-D symmetry breaking appears to be essential to enable this volumetric mixing.

Note, however, that recent 3-D simulations including viscosity have shown that small-scale mixing should be viscously damped in NIF hot spots[37,38,13]. This viscous dissipation would inhibit the fine-scale stirring necessary for the ablator material to mix atomically through the hot spot, as required to reproduce the observed x-ray emission. On the other hand, it is possible that molecular diffusion (not included in these HYDRA simulations) could spread the

ablator material through the hot spot once it is introduced source of the heavy hot spot contamination on N120405.

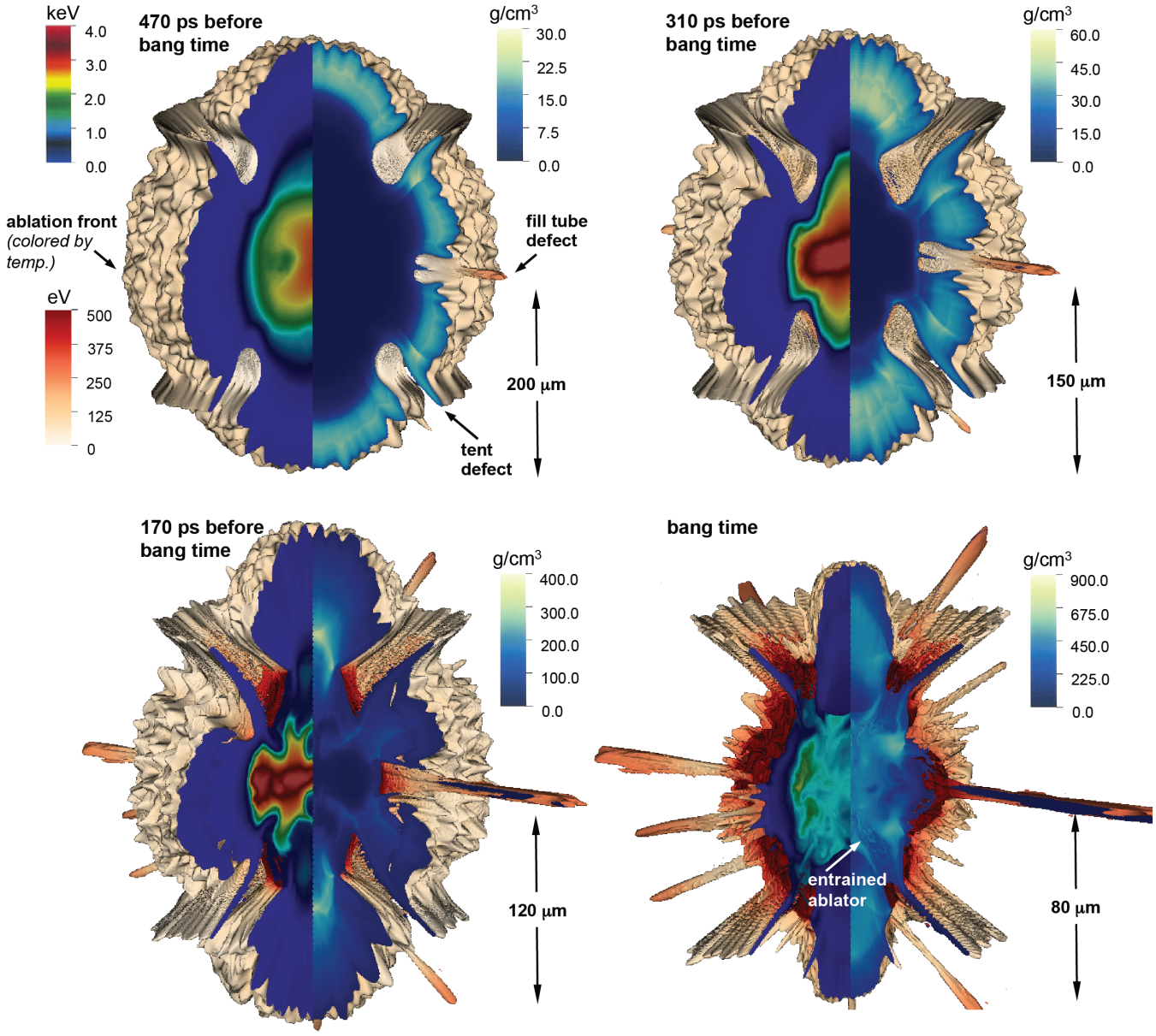

FIG. 4. (Color online) Stagnation sequence from the 3-D simulation of N120405. The renderings and color scales are analogous to those used in Fig. 2. The dynamics of the implosion are broadly similar to those from N120321, though the higher x-ray drive and higher velocity of this implosion has resulted in even more ablation front instability growth. Whereas the tent perturbation in N120321 clipped the north and south poles of the hot spot and substantially reduced the hot spot volume, here the tent perturbation reaches the very center of the implosion and ejects the hot spot to one side. In the process ~500 ng of ablator material is drawn into the hot spot. As a consequence of this mix, while N120321 was able to reach a central ion temperature of ~3 keV, N120405 reaches a temperature of only 1.5 keV.

via the tent defect. Alternately, it is also possible that the high hot spot temperature that leads to the high hot spot viscosity does not arise until after the ablator material has already been mixed into the DT. The complex effects that could be involved in this process are the subject of ongoing simulations, and clearly more work is required[39].

Finally, it is equally important to emphasize that these results do not represent proof that the tent defect was the Experimental confirmation of this route as the origin of the mix mass would be extremely challenging, and only a sequence of repeated experiments with reduced x-ray drive or a reduced tent perturbation could be conclusive that the tent is in fact the source. Nevertheless, it is compelling that this pair of 3-D simulations seems to reproduce the divergent behavior seen with N120405 and N120321 and implicates the tent as the culprit.

TABLE II. Summary of low foot simulation results.

	N120321			N120405		
	2-D	3-D	expt.	2-D	3-D	expt.
hot spot mix (ng)	50[¶]	50[¶]	0 – 75	750[¶]	750[¶]	500 – 725
bang time (ns)	22.86	22.85	22.91±0.04	22.57	22.53	22.70±0.08
burn width (ps)	150	167	158±40	82.1	130	161±40
x-ray P_0 (μm)	20.8	21.9	20.1±1.4	21.4	23.9	23.4±0.85
x-ray M_0 (μm)	17.4	19.8	22.7±2.7	13.8	24.1	26.5±4.0
PNI P_0 (μm)	—	24.4[§]	26±3	—	25.4[§]	27±3
DSNI P_0 (μm)	—	38.4[§]	35±3	—	31.7[§]	43±6
T_{ion} (keV)	2.9	2.6[§]	3.1±0.4	1.8	1.7[§]	1.69±0.13
DSR (%)	6.2	5.0[§]	6.2±0.6	5.7	5.5[§]	5.14±0.29
$Y_{13-15\,MeV}$	1.1×10^{15}	6.0×10^{14}	$4.2\pm0.1 \times 10^{14}$	3.0×10^{14}	1.4×10^{14}	$1.3\pm0.1 \times 10^{14}$

[¶] pre-loaded in DT gas
[§] from single-time post-processing at bang time

Table II summarizes quantitatively the 2-D and 3-D simulation results for the two low foot shots as compared to the experimental data. In the table, the x-ray image sizes are given in terms of their lowest order Legendre moments P_0 and M_0 from the waist and pole, respectively. Similarly, the Primary Neutron Image (PNI) and Down-Scattered Neutron Image (DSNI)[40] sizes are also characterized by their lowest order Legendre moments. Generally, the agreement is fair to good between both the 2-D and 3-D results and the data, except in the yield. For both N120321 and N120405, the 3-D simulations represent a factor of two degradation in yield compared to 2-D, and only these simulations are close to matching the measured yields. For several of the observables in Table II, even the 3-D simulation results do not overlap the experimental error bars; however, in these cases, most of the simulation results are within two error bars of the data. It is notable that, in addition to improving agreement with the measured yield, the 3-D simulation of N120405 also substantially improves the agreement with the measured burn width and x-ray M_0.

Note that, as indicated by the footnotes in Table II, the simulated hot spot mix mass quantities listed in the first row of the table are mix masses that must be pre-loaded into the simulation at initialization and are not simulation outputs like the other quantities. It is necessary to pre-load the ablator material in these simulations as HYDRA's interface tracking algorithm preserves pristine boundaries between materials. That is, material that is initially DT remains pure DT, and material that is initially CH remains purely CH even though it may be entrained by the tent perturbation and brought deep into the hot spot. There is currently no capability in 3-D HYDRA simulations to mix the two materials atomically over time as should happen in reality and is necessary to reproduce the hot spot radiative properties. The only recourse, then, is to mix them statically from the start of the simulation[41]. It is nevertheless notable that the pre-loaded mix mass that leads to good agreement with experimental yields in Table II is in agreement with the mix mass inferred experimentally.

A caveat also applies to the neutron image sizes, burn-weighted ion temperatures, and DSR values listed in Table II. Given the scale of these 3-D simulations, current computing resources do not allow running HYDRA with its inline Monte Carlo neutronics package, as is routinely done in 2-D simulations. The values in Table II are hence the results of instantaneous post-processing of the simulation results at bang time. As such, they represent a snapshot of the neutronics results from the simulations at peak neutron production and do not account for the time averaging over the burn as is included when running the neutronics inline. This may account for the simulated DSR and ion temperature being low relative to the data for N120321, and the DSNI P_0 being anomalously small for N120405, although these effects are difficult to quantify. Running 3-D simulations with the converged grid resolution used here and also using the inline neutronics package is a high priority for future modeling development and a subject of ongoing work. In all cases, the simulation results give a value for the DSR and ion temperature averaged over the 4π solid angle. Likewise, the experimental DSR and ion temperature values listed in the table are the average of the four neutron spectrometers fielded with these shots.

Finally, with respect to the understanding of low foot implosion performance, it deserves note that recent experiments testing a modified pulse shape corroborate the results described here. This modified pulse shape derived from a study of pulse shapes intermediate between the low foot pulse shape of the NIC and the high foot pulse shape by aiming to combine the best properties of both: a low fuel adiabat for good compression like the low foot and good ablation front stability for a robust implosion like the high foot[42]. Subsequent, keyhole[43] and HGR experiments[44] using this pulse shape confirmed both its low adiabat and its good stability characteristics similar to the high foot. Inflight radiography meant to assess the inflight implosion shape, then showed that the tent "scar," a visible imprint due to the tent readily identifiable in low foot implosions but undetectable in high foot implosions, was nearly invisible for the modified pulse shape[46]. Finally, a DT-layered implosion with this pulse shape demonstrated a 3–10× yield

improvement over comparable low foot implosions without compromising fuel compression[45]. This sequence of four shots confirms the essential result here, namely that the perturbation caused by the support tent, a perturbation visibly removed from inflight radiographs with the revised pulse shape, was a substantial source of yield degradation (~ 10×) for low foot-type implosions. Importantly, this yield enhancement was demonstrated without sacrificing compression and convergence, as in high foot implosions, and hence isolates the significance of ablation front instability growth as the source of yield degradation in low foot implosions as opposed to their higher compression. Equally importantly, these experiments also demonstrated that correct pulse shaping can substantially mitigate these tent effects and suggest a pathway to the stable, high-compression implosions necessary for ignition.

III. HIGH FOOT SIMULATIONS

The results of the 3-D simulation of the high foot implosion N130927 are shown in Fig. 5. The time sequence and color scales are analogous to those for the low foot implosions shown in Figs. 2 and 4. The contrast in the results, however, is striking. Unlike the low foot simulations of N120321 and N120405, the simulation of N130927 shows the effect of a much more stable ablation front. The large and dominating effect of the tent seen with the low foot is substantially reduced, as are the perturbations from the fill tube and the random modulations of the ablation front due to surface roughness. The different low-mode shape due the hohlraum flux asymmetries for this high foot implosion is also evident. While the low foot implosions tended towards very prolate shell shapes (though the hot spot shape is still oblate due to the tent perturbation), this high foot implosion is very oblate in the dense shell with high density caps of DT fuel accumulated at either pole. At bang time, this oblate shell shape now dominates the perturbation of the hot spot, though the defect from the tent perturbation is still visible. Despite this large P_2 asymmetry, comparing to the bang time rendering from Fig. 2 for N120321, a much larger, hotter, and generally more robust hot spot has formed. While N120321 only barely reaches a hot spot temperature of 3 keV in a small central pocket bounded by the polar tent perturbations, N130927 produces a large volume with a temperature greater than 4 keV. This higher hot spot temperature is substantially due to the reduced perturbation from the tent but also due to the significantly higher implosion velocity reached with the higher power and energy of N130927.

Another distinctive effect of the low-mode hohlraum flux asymmetries is seen in the evolution of the dense shell material through bang time to the final time of the simulation, 90 ps after bang time. From 260 ps and 80 ps before bang time to bang time, the mass accumulating at either pole can be seen to form paired spikes penetrating the hot spot from above and below. Shortly after bang time (not shown), these spikes collide and "ricochet" off of one another due to a slight left-right asymmetry in the hohlraum x-ray flux. This produces a strong jet of low density, hot spot plasma flowing at a roughly 45° angle toward the lower left. As seen in the final time rendering in Fig. 5, this jet breaks through the dense shell via the weak spot formed from the combined hohlraum flux asymmetries and tent perturbation. High velocity jets of hot plasma have been inferred from neutron time-of-flight (NTOF)[47] data for several NIF shots and, interestingly, are often inferred to be directed at an approximately 45° angel towards the south pole. The precise mechanism for the formation of this jet and its potential signatures in NTOF data are still under investigation, but it is notable that this simulation reproduces this characteristic feature seen on many NIF experiments. It is notable as well that this jetting behavior is a uniquely 3-D phenomena that cannot be captured in 2-D simulations.

Like Fig. 3, Fig. 6 shows the relative importance in terms of yield degradation of the various perturbation sources in 2-D simulations of N130927. In this case, the symmetric, unperturbed neutron yield is simulated to be 2.0×10^{17}. For N130927, the hohlraum flux asymmetries alone result in a 20× reduction in yield to 1.0×10^{16}, while the tent perturbation alone results in a 5× reduction to 3.9×10^{16}. This is in contrast to the results for the low foot N120321. While the tent was the dominant perturbation source for N120321, followed by the hohlraum asymmetries, those roles have reversed for N130927, and the large hohlraum asymmetry appears to dominate. This change in relative importance is to be expected based on the appearance of the 3-D simulation results in Fig. 5. There, the tent defect appears as a small perturbation atop the much larger low-mode asymmetry of the hot spot, in contrast to Fig. 2 where the tent dominates. The same ordering is also apparent in the insets in Fig. 6 where the tent alone only slightly distorts the hot spot shape but the flux asymmetries cause very large jets to completely penetrate the hot spot from above and below. It is notable, however, that even the seemingly minor perturbation from the tent still results in a factor of five degradation in yield. This high sensitivity to slight hot spot distortions is characteristic of the threshold of α-particle self-heating. That is, for this high velocity implosion that is on the edge of the regime for bootstrap self-heating, even small perturbations can substantially impact the yield.

The remaining three columns in Fig. 6 show the results with all 2-D perturbations included (a 30× yield reduction to 6.3×10^{15}), all 3-D perturbations included (a 60× yield reduction to 3.1×10^{15}), and finally the experimental result (a yield of 4.5×10^{15} amounting to a 45× reduction from the symmetric simulation). It is interesting that, like the low foot results, the 3-D simulation with all perturbations included results in roughly half the simulated yield of the 2-

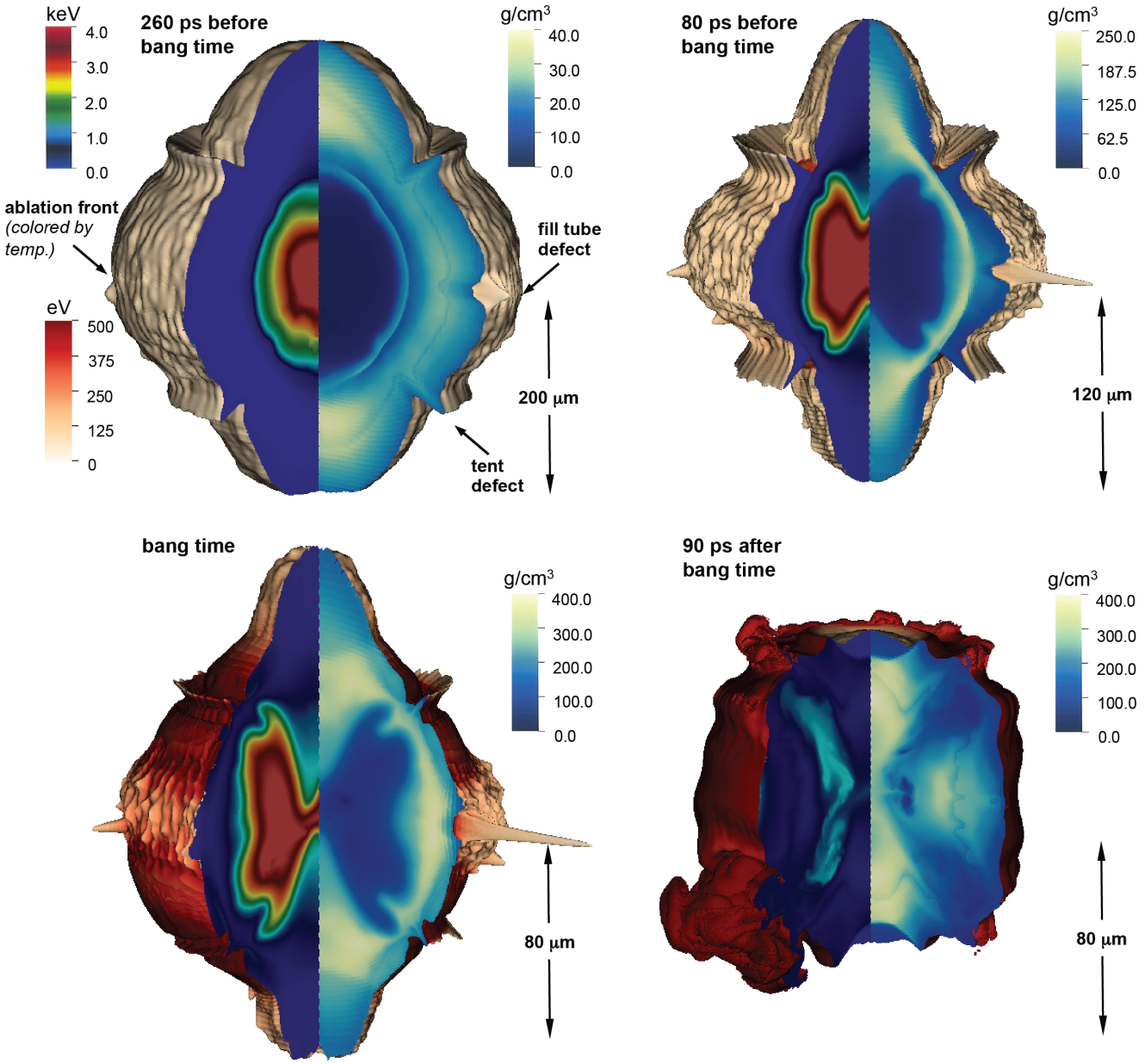

FIG. 5. (Color online) Stagnation sequence form the 3-D simulation of high foot shot N130927 using analogous renderings and color scales as in Fig. 2 and 4. Comparing to Figs. 2 and 4, this high foot implosion is clearly much less perturbed. Although still present, the tent perturbation is much reduced, as is the impact of surface roughness, and this implosion is more dominated by the low-mode asymmetry imprinted from the hohlraum flux asymmetries. Although the shell reaches significantly lower densities than in the low foot cases, the simulation shows a much larger, hotter, and generally more robust hot spot, leading to a much higher yield. Interestingly, in the last snapshot, the hot spot can be seen to disassemble by a strong jet moving to the lower left through the combined weak spot in the shell formed from the low-mode asymmetries and the tent perturbation. Neutron time-of-flight diagnostics have shown evidence of similar jets in this and other NIF implosions.

D equivalent. In contrast to the low foot results, however, the 2-D and 3-D simulation results now seem to straddle the measured yield value. As discussed further below, this could be an indication of the 3-D simulation being "over perturbed" in the sense of the flux asymmetries or tent perturbation being overestimated in the simulation, or could be an indication of a discrepancy in the underlying physical models used in the simulation. In comparing to Fig. 3, it is also interesting that the 3-D-to-1-D simulated yield degradation is actually larger for this high foot implosion (60×) than it is for the low foot implosion N120321 (50×). This lower 3-D yield relative to the unperturbed simulation is likely again evidence of the threshold of α-particle self-heating where the effect of even small perturbations can be magnified due to the quenching of bootstrap self-heating.

As discussed in Sec. I, shot N140819 was the highest power, thinnest shell implosion tested during the high foot campaign. Previous high foot shots had shown an increase

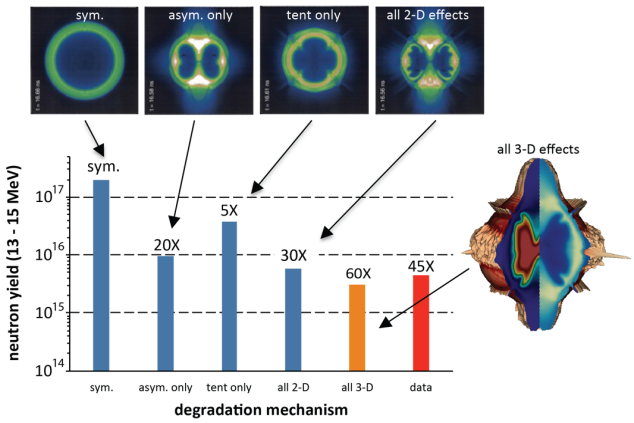

FIG. 6. (Color online) Relative impact of each perturbation source on neutron yield from 2-D simulations of N130927, as well as the 3-D simulation and experimental yields. The insets show the density distributions from 2-D simulations at bang time and the 3-D simulation result. In contrast to the low foot N120321 where the tent was the dominant source of yield degradation followed by the hohlraum flux asymmetries, here those roles are reversed. The hohlraum asymmetries result in a factor of twenty reduction in yield, while the tent is only a factor of eight. The visibly smaller hot spot distortion due to the tent as compared to the asymmetries is apparent in the insets. Interestingly, for this shot, the 2-D simulation including all effects is close to matching the experimental yield, while the 3-D simulation actually under-predicts the yield.

in performance with increasing power and energy and with thinner shells. For this thinnest and highest power shot, however, a drop in performance was observed. Based on extrapolation from the results of previous, lower power implosions with the same 165 μm ablator thickness, this 1.8 MJ implosion was expected to give a neutron yield greater than 1.0×10^{16}, but the experimental yield was half of this value at 5.5×10^{15}. Hot spot x-ray self-emission measurements indicated no mixing of ablator material into the hot spot, as was the experience with the highest power low foot implosions, and suggested that a different mechanism was responsible for the performance degradation.

As already noted, prior to this shot, a sag or "melt feature" was observed in the shell, believed to be due to the ultraviolet irradiation of the shell used in curing the epoxy applied to the fill tube attachment. It was hypothesized that this melt feature could have caused a rupturing of the shell during stagnation that could have resulted in the observed reduction in yield. It is also possible that the reduced ablator remaining mass could have increased the fuel pre-heating and adiabat and thereby reduced the compression and yield; however, the simulated 1-D adiabat values in Table I suggest that the adiabat for N140819 was no higher than for N130927 and that this should not have been an important effect. Another hypothesis was that with this very thin ablator and very high power, a highly unstable Atwood number could have developed between the DT fuel layer and the CH ablator resulting in a turbulent mix layer that could degrade both the fuel compression (also observed) and the neutron yield[48,49]. A final possibility was simply that the very low remaining ablator mass in this implosion reduced the 1-D confinement sufficiently to reduce the yield relative to thicker ablator shots with more remaining mass. While the latter two possibilities can be assessed in 1-D and 2-D simulations, and are discussed more in Sec. IV below, properly assessing the impact of the melt feature in concert with the support tent, fill tube and other perturbation sources, requires a 3-D simulation.

Details of the melt feature for shot N140819 are shown in Fig. 7. The upper left image shows the "low-mag" imaging used to assess the DT ice layer quality prior to the shot[33] where the melt feature was first detected. The image is "unrolled" into radius versus azimuthal angle, and the melt feature is visible as the wrinkle in the shell radial position between 260° and 360°. Note that the melt feature distorts the entire thickness of the shell and is not a modulation on the surface but a genuine wrinkle in the aggregate shell radius. Note also that the feature is roughly coincident with the fill tube location as shown in the lineout of the ablator inner radius below. This wrinkle in the CH-DT radius may be fit fairly well with a simple function as shown. When this approximate perturbation is applied in a 3-D HYDRA simulation in the correct orientation with the support tent, fill tube, etc., the initial conditions are as shown in the rendering on the right. Here the color scale gives the deviation in height over the surface of the capsule, and the hohlraum axis is roughly vertical. Though the surface roughness and surrogate tent and fill tube perturbations are included in the initialization of the ablator surface, it is clear from the figure that they are dwarfed by the melt feature perturbation. The tent perturbation is barely discernable above and below the melt feature and emphasizes the 3-D character of these two perturbations in combination. Given its large amplitude (even compared to the tent perturbation), it might be expected that this melt feature dominates the implosion dynamics. On the other hand, the melt feature is very long wavelength in character and should grow very slowly so that only a small final distortion results.

The relative growth of these combined features (melt feature, tent, fill tube, surface roughness, and hohlraum asymmetries) is shown in the 3-D simulation sequence in Fig. 8. Unlike the implosion results shown in Figs. 2, 4, and 5, Fig. 8 shows only the ablation front in order to emphasize the impact of the melt feature. The usual features of the tent and fill tube can be identified, while the melt feature can be seen as the large but shallow ring passing through the fill tube and the upper and lower tent defects in the first three snapshots of the figure. As anticipated, the melt feature grows much more slowly than the other surface perturbations due to its dominantly longer wavelength content and is exceeded in amplitude by the initially smaller tent perturbation for all times shown in the figure. By bang time, however, the thinning of the shell has allowed the stagnation shock to break out earlier in the location of the melt ring suggesting a decrease in confinement with this long wavelength perturbation. In the final snapshot shown,

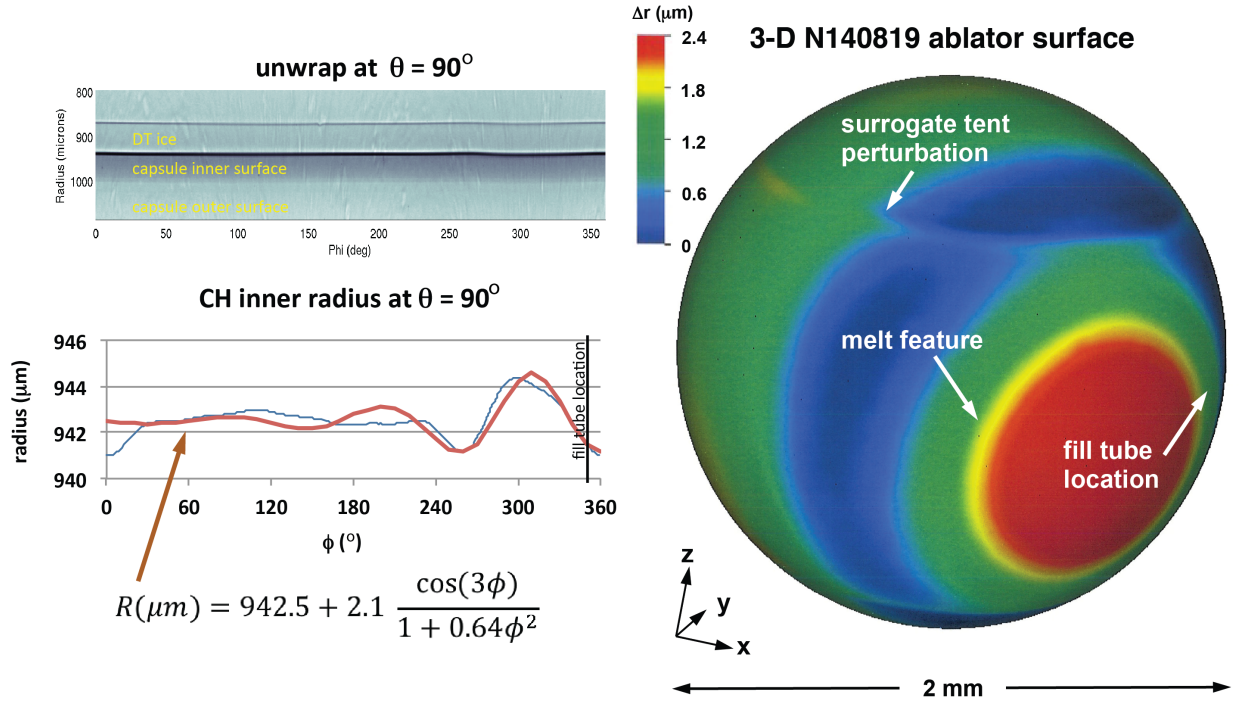

FIG. 7. (Color online) Details of the capsule "melt feature" from shot N140819. The upper left image is taken from the "low-mag." imaging system used to assess the DT ice layer quality prior to the implosion. The sag affecting both the shell and the ice layer is clearly visible between 260° and 360° in this image. A lineout of the CH ablator inner radius versus angle is shown in the lower left with an approximate fit to the observed modulation. Applying that approximate fit in a 3-D HYDRA simulation results in the initial ablator surface height map shown on the right with the color scale showing the deviation in height around the capsule. Although typical surface roughness and tent perturbations are included in this simulation, they are dwarfed by the large, low-mode melt feature.

140 ps after bang time, a residual ring shape is still apparent, but the implosion still appears to be disassembling in a fairly symmetric fashion.

A clearer indication of the importance of the melt feature can be gained by comparing 2-D simulations omitting the melt feature to the 3-D results. (Note that there is no satisfactory way to include the melt feature in 2-D in the presence of the tent). Results for both high foot implosions are summarized in Table III including 2-D and 3-D simulations. First, for the lower power and thicker shell implosion N130927, the 2-D and 3-D results are broadly similar. Notably, the 3-D simulation shows closer agreement for the burn width, the x-ray M_0, and also the DSR than the 2-D simulation does. As noted above, the 2-D and 3-D simulations straddle the experimental yield, while the slightly higher temperature of the 2-D simulation is closer to the experiment. Like the 3-D low foot results, the neutronics results reported here for the 3-D simulations result from instantaneous post-processing at bang time and hence omit the averaging over the burn duration that is included in the 2-D results. It is surprising nonetheless how well the 3-D result matches the experimental DSR measurement, while the 2-D result is significantly higher. Whether this improved agreement is a genuine 3-D versus 2-D effect or an artifact of the post-processing can only be resolved by further improvements in simulation capabilities.

The 3-D simulation results for N140819 show similarly good agreement with the measurements, with the exception of the 3-D simulated neutron image sizes being significantly smaller than the experimental data or 2-D results. This again may be an artifact of the post-processing. As with N130927, the 3-D results show better agreement with the measurement for the DSR. Also like N130927, the 2-D and 3-D results under-predict the burn-averaged ion temperature, but, unlike N130927, there is a substantial difference in 2-D versus 3-D simulated yields with only the 3-D result close to the data. This could indicate that the melt feature was responsible for the observed performance of N140819. However, given that this feature can only be correctly included in a 3-D simulation and certainly couples to the other perturbation sources, its individual impact is difficult to assess. A 2-D simulation with the melt feature alone showed almost no degradation in yield compared to the symmetric result, while the tent and flux asymmetries individually both resulted in a factor of ten reduction in yield. This suggests that, at worst, only the melt feature in combination with other perturbations leads to the observed yield degradation.

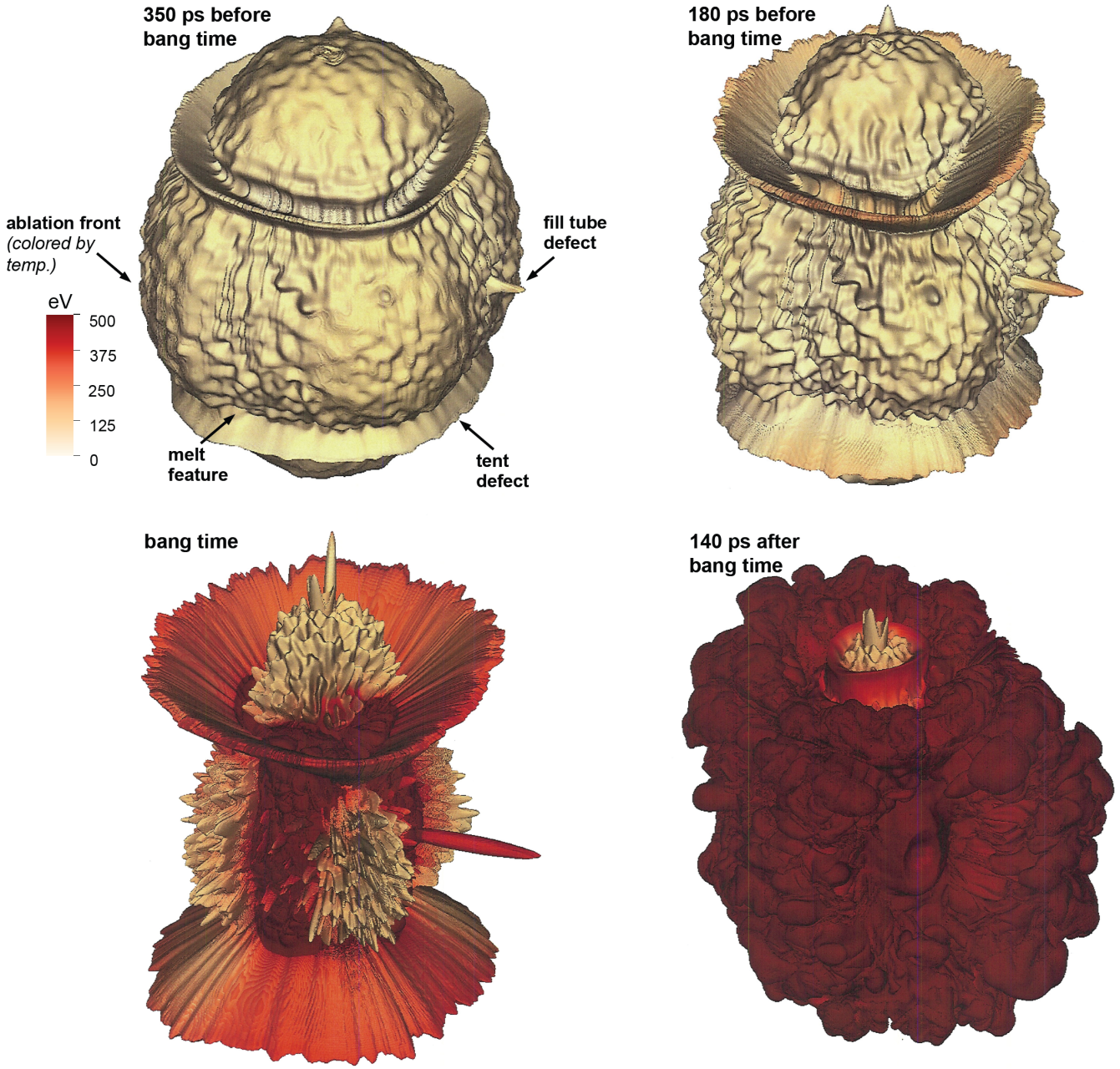

FIG. 8. (Color online) Stagnation sequence from the 3-D simulation of N140819. Unlike Figs. 2, 4, and 5, only the ablation front is shown in these renderings. The usual tent, fill tube, and surface roughness features are visible. The effect of the melt feature can be seen as a ring on the right half of the renderings coincident with the fill tube defect. The thinning of the shell due to this feature results in the stagnation shock breaking through the shell earlier in the location of the ring as seen at bang time. After bang time, a residual ring shape is still apparent, but the implosion appears to disassemble in a fairly symmetric fashion.

A more general sense of why the yield and other performance metrics decreased for N140819 compared to other high foot implosions is suggested by Fig. 9. Fig. 9 contrasts the thin shell, high power high foot implosion N140819 against the results for the high compression low foot implosion N120321. What is striking in comparing these two simulations is that the high foot implosion, despite its lower compression, has reached a similar level of perturbation to the low foot implosion. The prolate shape of the two implosions is surprisingly similar, and, more surprisingly, the tent and other perturbation sources have been amplified to a remarkably similar, if not greater, extent. As can be seen from the color scales, the high foot implosion reaches a significantly higher hot spot temperature (~5 keV as compared to ~3 keV for the low foot simulation) but at a significantly lower shell density (~400 g/cm^3 as compared to ~600 g/cm^3). This higher hot spot temperature is reached despite the similar level of shell

perturbations and is indicative of the tradeoff made in the high foot implosion. That is, by sacrificing fuel adiabat and compressibility, the high foot implosion does not reach the perturbation levels of the low foot until much higher velocities (319 compared to 390 km/s). In this case, the higher velocity of the high foot implosion outweighs the higher compression of the low foot such that the high foot achieves significantly higher yield.

TABLE III. Summary of high foot simulation results.

	N130927			N140819		
	2-D	3-D	expt.	2-D	3-D	expt.
hot spot mix (ng)	0[¶]	0[¶]	0 – 150	0[¶]	0[¶]	0 – 150
bang time (ns)	16.56	16.53	16.59±0.03	15.21	15.16	15.14±0.03
burn width (ps)	120	143.5	188±30	100	110	147±30
x-ray P_0 (μm)	31.2	31.4	35.3±3.0	30.9	30.5	31.3±2.2
x-ray M_0 (μm)	39.8	45.7	49.8±1.5	29.5	28.8	29.9±1.0
PNI P_0 (μm)	33.7	27.7[§]	32±4	35.6	25.3[§]	33.4±3
DSNI P_0 (μm)	53.6	51.1[§]	55±4	54.7	33.3[§]	46.7±6
T_{ion} (keV)	4.1	3.9[§]	4.43±0.15	4.5	4.4[§]	5.5±0.2
DSR (%)	4.7	3.5[§]	3.48±0.17	4.4	3.9[§]	3.5±0.2
$Y_{13-15\,MeV}$	6.3×10^{15}	3.1×10^{15}	$4.5\pm0.1 \times 10^{15}$	1.3×10^{16}	4.3×10^{15}	$5.5\pm0.1 \times 10^{15}$

[¶] pre-loaded in DT gas

[§] from single-time post-processing at bang time

The likely explanation for why N140819 experienced a degradation in performance relative to other high foot implosions thus appears to be the reemergence of large ablation front perturbations at higher velocities, again primarily due to the tent. The melt feature may also have contributed, although 2-D simulations suggest this was at worst a secondary effect. In a more general sense, this high power, thin shell high foot implosion brought the high foot platform full circle. After reducing the ablation front perturbations to a much tamer level with its strong first shock, as seen with N130927, N140819 was accelerated sufficiently strongly that it returned to the perturbation levels of N120321 and began to experience a similar degradation in yield. Recalling that N120405, the higher power companion to N120321, mixed heavily, N140819 may indeed have been on the edge of a very steep performance cliff.

IV. HIGHER RESOLUTION 2-D SIMULATIONS

It was noted in Sec. I that 2-D hohlraum simulations of the high foot implosion series consistently over-predicted the DSR measurements for these shots. A similar over-prediction of the DSR can be seen in the 2-D simulation results listed in Table III. Given this consistent over-prediction, it has been speculated that additional effects are present in high foot implosions, beyond those included in 2-D simulations of the type summarized in Tables II and III. In particular, it has been hypothesized that significant supra-thermal electron pre-heating[50] could be occurring raising the DT fuel adiabat and reducing its compressibility. Another hypothesis is that the strongly driven high foot implosions are impacted by significant mixing at the fuel-ablator interface that could also heat the DT fuel and reduce its compressibility. This scenario seems particularly plausible given that all high foot implosions have been shot with "1X" Si dopant in the CH ablator, while most of the highest power low foot implosions (that do not show such a discrepancy between measured and simulated DSR) were shot with "2X" Si dopant. The higher "2X" dopant in the low foot implosions maintains a more stable Atwood number at the fuel-ablator interface and hence mitigates this internal fuel-ablator mix. Note that the higher adiabat of the high foot implosion confers no improvement in stability at the near-classically unstable fuel-ablator interface.

It is interesting that the 3-D results in Table III do not appear to show a very significant discrepancy in the simulated DSR. However, as discussed in Sec. II, these DSR values are computed from single-time post-processing of the 3-D simulations and hence are not properly time-averaged, as the 2-D results are, for comparison to the experimental data. This ambiguity leaves open the possibility that the DSR values in the 3-D simulations, like the 2-D simulations, are over-predicted relative to the data. These considerations motivate some assessment of the hypotheses for a reduced DSR as seen in experiments. The possibility of supra-thermal electron pre-heating of the fuel is under active investigation in simulation[51], and this hypothesis will not be discussed further here. Short wavelength fuel-ablator mixing, however, fits readily within the simulation paradigm discussed above and an assessment of its impact is made here.

Fig. 10 shows 2-D simulations of short wavelength fuel-ablator mixing in the four implosions discussed above (the low foot implosions N120321 and N120405, and the high foot implosions N130927 and N140819). Each of the four panels shows a 2-D simulation run on a 15° wedge of the capsule with resolution sufficient to resolve modes $\ell = 12 - 1{,}200$. Past convergence tests have shown this range of modes to be sufficient to resolve whether significant fine-scale mixing develops at this interface. In each case, the

development of the instabilities is shown at the end of the acceleration phase (time of peak implosion velocity) when any mix layer should be well developed. While the two high foot cases do show somewhat more structure at the fuel-ablator interface than is seen in the low foot cases, the extent of this mixing is relatively minor. Past experience has shown that near 100% mixing of the DT fuel with the ablator (for example, as seen in Fig. 6 of Ref. 49) is necessary to have a noticeable impact on the simulated DSR. Even in the case of the high power, thin shell N140819, no secondary Kevlin-Helmholtz instabilities[52,53] or other nonlinear mixing signatures are apparent, and the impact on the DSR due to this mixing is expected to be negligible.

Of course, more mixing can be expected in 3-D reality than in the 2-D approximation represented in these simulations. However, earlier 3-D simulation studies[49] of implosions with similar fuel-ablator Atwood numbers and similar weakly nonlinear 2-D growth suggest that the mixing in 3-D should not be significantly greater than in 2-D in this case. Hence, unless some other effect significantly changes the Atwood number predicted in these simulations, extensive fuel-ablator mixing is an unlikely explanation for any possible discrepancy in high foot DSR measurements.

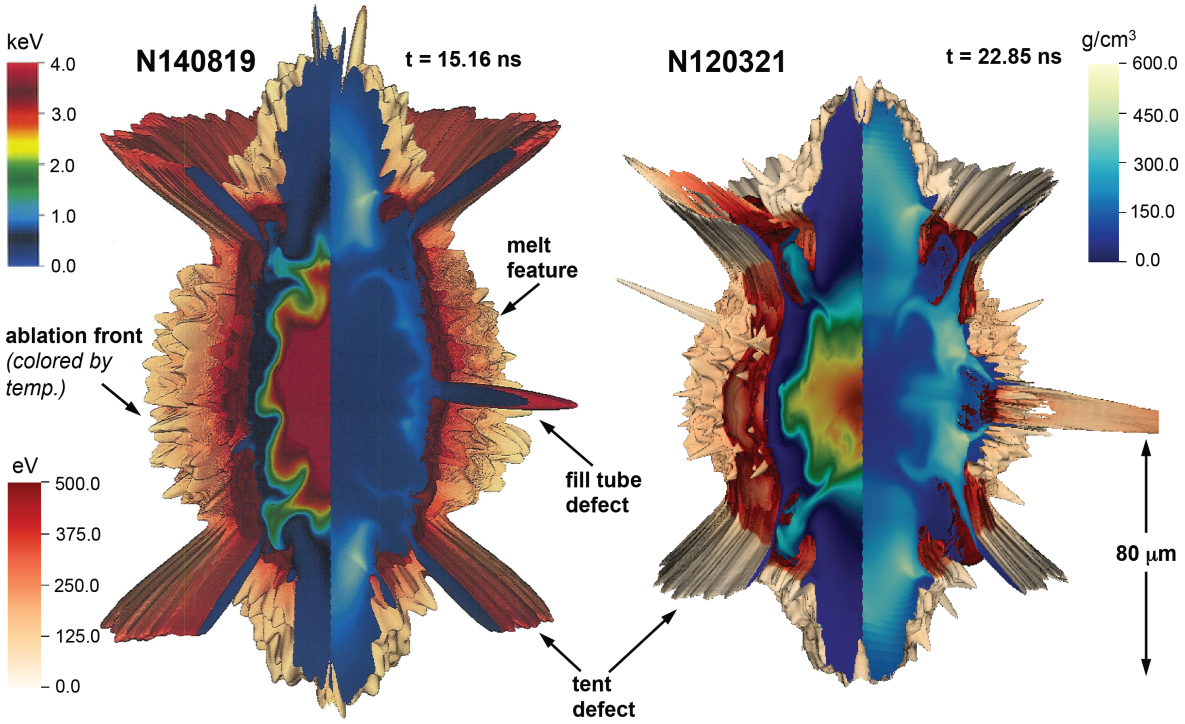

FIG. 9. (Color online) Comparison of bang time renderings of the high foot shot N140819 and the low foot shot N120321. Both simulations are shown on the same color scales. The N140819 simulation reaches a much lower shell density compared to N120321 but also a much higher hot spot temperature accounting for its much higher yield. It is noteworthy, however, that despite its higher adiabat, N140819 has reached a similar level of shell distortion at bang time compared to N120321. The significantly higher velocity of N140819 apparently compensates for the high level of shell distortion and still enables this implosion to achieve significant yield. Nevertheless, like the low foot N120321, N140819 appears to be on the edge of a cliff in performance.

V. SUMMARY AND IMPLICATIONS FOR FUTURE EXPERIMENTS

This paper has summarized the status of detailed post-shot simulations of ignition implosions on the NIF using our current best understanding of the perturbation sources present in these implosions and best practice simulation technique. Two low foot shots from the NIC and two high foot shots from experiments following the NIC have been simulated in detail. These shots span much of the range of ignition implosion experiments so far tested on NIF, from the very high compression implosions tested during the NIC to the lower compression but significantly higher yield implosions from the subsequent high foot campaign. For all four shots simulated, a reasonable, albeit not perfect, level of agreement is found with the data. For many of the observables, the experimental results are matched within the error bars or only just outside of the error bars. For such highly nonlinear quantities like the neutron yield, the simulation results vary from 30% too high relative to the data, to matching the data within the error bars, to 30% too low relative to the data, and 20% too low relative to the data. It is arguable that this may be the best agreement possible given the imperfect knowledge of initial and boundary conditions in these experiments.

For both of the low foot implosions simulated, the implosion performance is dominated by the very large ablation front perturbation seeded by the capsule support tent. In the extreme case, the tent perturbation not only

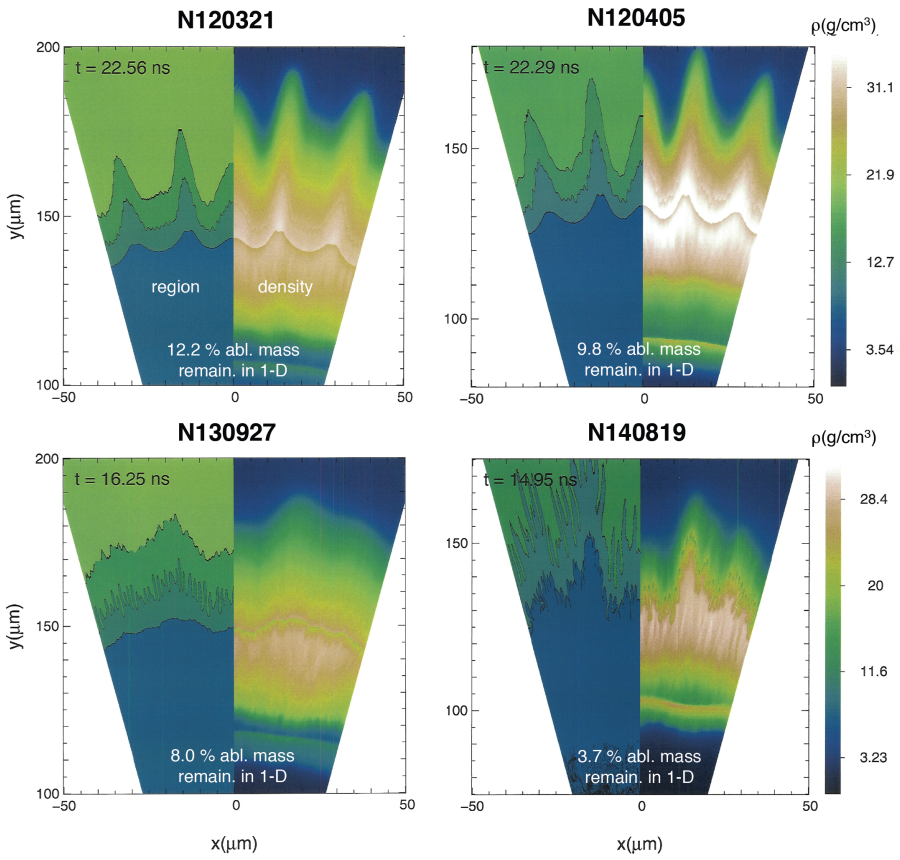

FIG. 10. (Color online) Comparison of 2-D high mode (ℓ = 12 – 1,200) simulations of the two low foot and two high foot shots simulated in 3-D above. The left half of each panel shows the material region with blue representing DT fuel and green representing the various CH dopant layers. The right half in each panel shows the density with the color scale on the right. These simulations have sufficient resolution to capture any high mode mixing that can occur between the CH ablator and DT fuel and are shown at their respective times of peak implosion velocity when any mixing layer should be well developed. The two low foot shots (N120321 and N120405) are dominated by growth at the ablation front with little growth developing local to the fuel-ablator interface. The high concentration of silcon dopant in the inner part of the ablator for these shots ("2X" versus the "1X" used in the high foot shots) maintains a nearly stable Atwood number at the fuel-ablator interface throughout the implosion resulting in little fuel-ablator local mixing. The lower dopant concentration, lower remaining mass, and higher velocity of the two high foot implosions (N130927 and N140819) has led to more instability growth at the fuel-ablator interface but is not sufficient to significantly impact the expected DSR.

truncates the hot spot by clipping off its upper and lower ends but also entrains ablator material deep into the hot spot to be mixed through the hot spot in a chaotic, 3-D manner. The heavy mixing of ablator material into the hot spot seen on several NIC shots appears to be due to this tent-related effect. For the moderately driven high foot implosion that was simulated, the effects of ablation front instabilities are substantially reduced compared to the low foot (the effect of the tent in particular), and the implosion performance is dominated by the low-mode asymmetry imprinted from the hohlraum. For the higher power, thinner shell high foot implosion, however, ablation front instabilities are simulated to have returned to a level of growth similar to the original low foot implosion, and the growth of the tent defect is remarkably reminiscent of that seen for the low foot. This appears to explain the reduction in performance seen with this highest power, thinnest shell high foot implosion compared to previous implosions. By trading compression for increased stability, however, this implosion did not reach this level of shell distortion until attaining a much higher implosion velocity compared to the low foot. The benefits of this higher velocity appear to have outweighed the deleterious effects of increased instability growth and enabled a higher yield. Nevertheless, these simulations suggest that this high foot implosion was on the edge of a cliff with respect to ablation front instability, similar to that seen with the low foot when driven to too high a velocity. Finally, for all four implosions simulated, high resolution 2-D simulations suggest that fuel-ablator mixing should not be playing a role in these implosions and indicate that any discrepancies in the simulated DSR are likely not due to short wavelength fuel-ablator mix.

While the agreement between simulation and experiment is broadly favorable for all four of the shots simulated, there remain some systematic discrepancies. In particular, for both of the high foot shots simulated, the burn-averaged ion temperatures are lower in simulation compared to the measured values. The discrepancy is relatively small (~20%) but is consistent for both shots. This effect has been noted for some time in 2-D simulations and for low foot as well as high foot implosions. In the case of the 3-D simulations presented here, it is interesting that both simulations also under predict the neutron yield. It is possible, then, to interpret these results as simply "over-perturbed." That is, given uncertainties in the magnitudes of the largest perturbing effects in these implosions, the hohlraum flux asymmetries and the tent, it is possible that one or both of these effects is overestimated in the current simulations leading to an under-prediction of the yields and ion temperatures. On the other hand, assuming that the perturbation sources are being modeled correctly, it is also possible that these simulations are suggesting a need to

modify the underlying physical models used in the simulations. For example, a reduction in the hot spot thermal conductivity in the simulations could compensate for both the low neutron yields and low ion temperatures relative to the data. It has long been speculated that self-induced magnetic fields or strong degeneracy effects could result in modified conductivities that could explain these results. Other physical model discrepancies, such as in electron-ion equilibration rates or charged particle stopping powers, are also possible. Futher simulation and experimental work is required to resolve whether such effects do in fact play a role.

Finally, these results have several implications for future experiments aimed at achieving higher implosion performance. Foremost they indicate that the highest power, thinnest shell high foot implosions were, like the low foot implosions, likely impacted by ablation front perturbations seeded by the support tent. This conclusion argues strongly for developing a less perturbative support mechanism as a rapid route to improving performance. Reviewing the 2-D high foot implosion results shown above, roughly a factor of two improvement in neutron yield is predicted if the tent perturbation were completely eliminated. Of course, no substitute capsule mounting will be perfectly non-perturbative, so this estimate is obviously an upper bound. As future implosions are again pushed to higher velocities, however, a reduced perturbation from the capsule mounting may yield ever greater performance benefits. A variety of schemes are under investigation, and there is optimism for at least substantially reducing the current impact from the tent.

These simulations also confirm that the low-mode flux asymmetries imprinted by the hohlraum significantly degraded the performance of high foot implosions. Managing the radiation flux asymmetries inside the hohlraum has been a subject of intensive effort since the beginning of NIF implosion experiments[54,55,56], and further experimental validation of the relative impact of low-mode asymmetries versus ablation front instabilities is required. Nevertheless, developing hohlraum designs with a more symmetric and more predictable radiation environment is strongly indicated. Efforts are underway to address both of these challenges. In particular, hohlraums designs are being developed with larger case-to-capsule ratios for reduced asymmetry imprint[57], as well as with lower gas fills that appear to give improved predictability compared to simulations[58].

ACKNOWLEDGEMENTS

This work was performed under the auspices of the U.S. Department of Energy by Lawrence Livermore National Laboratory under Contrac DE-AC52-07NA27344.

[1]J. D. Lindl, *Inertial Confinement Fusion: The Quest for Ignition and Energy Gain Using Indirect Drive* (American Institute of Physics, Woodbury, NY 1998).

[2]S. Atzeni and J. Meyer-ter-Vehn, *The Physics of Inertial Fusion* (Clarendon, Oxford, 2004).

[3]E. I. Moses, R. N. Boyd, B. A. Remington, C. J. Keane, and R. Al-Ayat, Phys. Plasmas **16**, 041006 (2009).

[4]M. J. Edwards, P. K. Patel, J. D. Lindl, L. J. Atherton, S. H. Glenzer, S. W. Haan, J. D. Kilkenny, O. L. Landen, E. I. Moses, A. Nikroo, R. Petrasso, T. C. Sangster, P. T. Springer, S. Batha, R. Benedetti, L. Bernstein, R. Betti, D. L. Bleuel, T. R. Boehly, D. K. Bradley, J. A. Caggiano, D. A. Callahan, P. M. Celliers, C. J. Cerjan, K. C. Chen, D. S. Clark, G. W. Collins, E. L. dewald, L. Divol, S. Dixit, T. Deoppner, D. H. Edgell, J. E. Rai, M. Farrell, R. J. Fortner, J. Frenje, M. B. Gatu Johnson, E. Giraldez, V. Yu. Glebov, G. Grim, B. A. Hammel, A. V. Hamza, D. R. Harding, S. P. Hatchett, N. Hein, H. W. Herrmann, D. Hicks, D. E. Hinkel, M. Hoppe, W. W. Hsing, N. Izumi, B. Jacoby, O. S. Jones, D. Kalantar, R. Kauffman, J. L. Kline, J. P. Knauer, J. A. Koch, B. J. Kozioziemski, G. Kyrala, K. N. LaFortune, S. Le Pape, R. J. Leeper, R. Lerche, T. Ma, B. J. MacGaowan, A. J. MacKinnon, A. Macphee, E. R. Mapoles, M. M. Marinak, M. Mauldin, P. W. McKenty, M. Meezan, P. A. Michel, J. Milovich, J. D. Moody, M. Moran, D. H. Munro, C. L. Olson, K. Opachich, A. E. Pak, T. Parham, H.-S. Park, J. E. Ralph, S. P. Regan, B. Remington, H. Rinderknecht, H. F. Robey, M. Rosen, S. Ross, J. D. Salmonson, J. Sater, D. H. Schneider, F. H. Séguin, S. M. Sepke, D. A. Shaughnessy, V. A. Smalyuk, B. K. Spears, C. Stoeckl, W. Stoeffl, L. Suter, C. A. Thomas, R. Tommasini, R. P. Town, S. V. Weber, P. J. Webner, K. Widman, M. Wilke, D. C. Wilson, C. B. Yeamans, and A. Zylstra, Phys. Plasmas **20**, 070501 (2013).

[5]O. A. Hurricane, D. A. Callahan, D. T. Casey, E. L. Dewald, T. R. Dittrich, T. Döppner, M. A. Barrios Garcia, D. E. Hinkel, L. F. Berzak Hopkins, P. Kervin, J. L. Kline, S. Le Pape, T. Ma, A. G. MacPhee, J. L. Milovich, J. Moody, A. E. Pak, P. K. Patel, H.-S. Park, B. A. Remington, H. F. Robey, J. D. Salmonson, P. T. Springer, R. Tommasini, L. R. Benedetti, J. A. Caggiano, P. Celliers, C. Cerjan, R. Dylla-Spears, D. Edgell, M. J. Edwards, D. Fittinghoff, G. P. Grim, N. Guler, N. Izumi, J. A. Frenje, M. Gatu Johnson, S. Haan, R. Hatarik, H. Herrmann, S. Khan, J. Knauer, B. J. Kozioziemski, A. L. Kritcher, G. Kyrala, S. A. Maclaren, F. E. Merrill, P. Michel, J. Ralph, J. S. Ross, J. R. Rygg, M. B. Schneider, B. K. Spears, K. Widmann, and C. B. Yeamans, Phys. Plasmas **21**, 056314 (2014).

[6]N. B. Meezan, L. F. Berzak Hopkins, S. Le Pape, L. Divol, A. J. Mackinnon, T. Döppner, D. D. Ho, O. S. Jones, S. F. Khan, T. Ma, J. L. Milovich, A. E. Pak, J. S. Ross, C. A. Thomas, L. R. Benedetti, D. K. Bradley, P. M. Celliers, D. S. Clark, J. E. Field, S. W. Haan, N. Izumi, G. A. Kyrala, J. D. Moody, P. K. Patel, J. E. Ralph, J. R. Rygg, S. M. Sepke, B. K. Spears, R. Tommasini, R. P. J. Town, J. Biener, R. M. Bionta, E. J. Bond, J. A. Caggiano, M. J. Eckart, M. Gatu Johnson, G. P. Grim, A.V. Hamza, E. P. Hartouni, R. Hatarik, D. E. Hoover, J. D. Kilkenny, B. J. Kozioziemski, J. J. Kroll, J. M. McNaney, A. Nikroo, D. B. Sayre, M. Stadermann, C. Wild, B. E. Yoxall, O. L. Landen, W. W. Hsing, and M. J. Edwards, Phys. Plasmas **22**, 062703 (2015).

[7]J. L. Kline, S. A. Yi, A. N. Simakov, R. E. Olson, D. C. Wilson, G. A. Kyrala, T. S. Perry, S. Batha, A. B. Zylstra, E. L. Dewald, R. Tommasini, J. E. Ralph, D. J. Strozzi, M. B. Schneider, A. G. MacPhee, D. A. Callahan, D. E. Hinkel, O. A. Hurricane, J. L. Milovich, J. R. Rygg, S. Khan, S. Haan, P. Celliers, D. Clark, B. Hammel, B. Kozioziemski, M. Marinak, H. G. Rinderknecht, H. Robey, J. Salmonson, P. Patel, T. Ma, J. Edwards, M. Stadermann, S. Baxamusa, C. Alford, M. Wang, A Nikroo, N. Rice, D. Hoover, K. Youngblood, H. Xu, H. Huang, and H. Sio, Phys. Plasmas, *submitted* (2015).

[8]M. M. Marinak, G. D. Kerbel, N. A. Gentile, O. Jones, D. Munro, S. Pollaine, T. R. Dittrich, and S. W. Haan, Phys. Plasmas **8**, 2275 (2001).

[9]S. R. Nagel, S. W. Haan, J. R. Rygg, M. Barrios, L. R. Benedetti, D. K. Bradley, J. E. Field, B. A. Hammel, N. Izumi, O. S. Jones, S. F. Khan, T. Ma, A. E. Pak, R. Tommasini and R. P. J. Town, Phys. Plasmas **22**, 022704 (2015).

[10]R. Tommasini, J. E. Field, B. A. Hammel, O. L. Landen, S. W. Haan, C. Aracne-Ruddle, L. R. Bendetti, D. K. Bradley, D. A. Callahan, E. L. Dewald, T. Döppner, M. J. Edwards, O. A. Hurricane, N. Izumi, O. A.

Jones, T. Ma, N. B. Meezan, S. R. Nagel, J. R. Rygg, K. S. Segraves, M. Stadermann, R. J. Strauser, and R. P. J. Town, Phys. Plasmas **22**, 056315 (2015).

[11]J. Edwards, M. Marinak, T. Dittrich, S. Haan, J. Sanches, J. Klingmann, and J. Moody, Phys. Plasmas 1**2**, 056318 (2005).

[12]D. S. Clark, D. E. Hinkel, D. C. Eder, O. S. Jones, S. W. Haan, B. A. Hammel, M. M. Marinak, J. L. Milovich, H. F. Robey, L. J. Suter, and R. P. J. Town, Phys. Plasmas **20**, 056318 (2013).

[13]D. S. Clark, M. M. Marinak, C. R. Weber, D. C. Eder, S. W. Haan, B. A. Hammel, D. E. Hinkel, O. S. Jones, J. L. Milovich, P. K. Patel, H. F. Robey, J. D. Salmonson, S. M. Sepke, and C. A. Thomas, Phys. Plasmas **22**, 022703 (2015).

[14]S. P. Regan, R. Epstein, B. A. Hammel, L. J. Suter, H. A. Scott, M. A. Barrios, D. K. Bradley, D. A. Callahan, C. Cerjan, G. W. Collins, S. N. Dixit, T. Döppner, M. J. Edwards, D. R. Farely, K. B. Fournier, S. Glenn, S. H. Glenzer, I. E. Golovkin, S. W. Haan, A. Hamza, D. G. Hicks, N. Izumi, O. S. Jones, J. D. Kilkenny, J. L, Kline, G. A. Kyrala, O. L. Landen, T. Ma, J. J. MacFarlane, A. J. MacKinnon, R. C. Mancini, R. L. McCrory, N. B. Meezan, D. D. Meyerhofer, A. Nikroo, H.-S. Park, J. Ralph, B. A. Remington, T. C. Sangster, V. A. Smalyuk, R. T. Springer, and R. P. J. Town, Phys. Rev. Lett. **111**, 045001 (2013).

[15]T. Ma, P. K. Patel, N. Izumi, P. T. springer, M. H. Key, L. J. Atherton, L. R. Benedetti, D. K. Bradley, D. A. Callahan, P. M. Celliers, C. J. Cerjan, D. S. Clark, E. L. Dewald, S. N. Dixit, T. Döppner, D. H. Edgell, R. Epstein, s. Glenn, G. Grim, S. W. Haan, B. A. Hammel, D. Hicks, W. W. Hsing, O. S. Jones, S. F. Khan, J. D. Kilkenny, J. L. Kline, G. A. Kyrala, O. L. Landen, S. Le Pape, B. J. MacGowna, A. J. Mackinnon, A. G. MacPhee, N. B. Meezan, J. D. Moody, A. Pak, T. Parham, H.-S. Park, J. E. Ralph, s. P. Regan, B. A. Remington, H. F. Robey, J. S. Ross, B. K. Spears, V. Smalyuk, L. J. Suter, R. Tommasini, R. P. Town, S. V. Weber, J. D. Lindl, M. J. Edwards, S. H. Glenzer, and E. I. Moses, Phys. Rev. Lett. **111**, 085004 (2013).

[16]T. R. Dittrich, O. A. Hurricane, D. A. Callahan, E. L. Dewald, T. Döppner, D. E. Hinkel, L. F. Berzak-Hopkins, S. Le Pape, T. Ma., J. L. Milovich, J. C. Moreno, P. K. Patel, H.-S. Park, B. A. Remington, and J. D. Salmonson, Phys. Rev. Lett. **112**, 055002 (2014).

[17]W. H. Goldstein, *Workshop on the Science of Fusion Ignition on NIF*, San Ramon, CA, May 22 – 24, 2012.

[18]R. D. Richtmyer, Commun. Pure Appl. Math. **13**, 297 (1960).

[19]E. E. Meshkov, Fluid Dyn. **4**, 101 (1969).

[20]Lord Rayleigh, *Scientific Papers* (Cambridge University Press, Cambridge, England, 1900).

[21]G. I. Taylor, Proc. R. Soc. London, Ser. A **201**, 192 (1950).

[22]A. L. Kritcher, D. E. Hinkel , D. A. Callahan, O. A. Hurricane, D. Clark, T. R. Dittrich, T. Döppner, M. J. Edwards S. Haan, L. F. Berzak Hopkins, O. Jones, O. Landen, T. Ma, J. L. Milovich, A. E. Pak, H.-S. Park, P. K. Patel, J. Ralph, J. D. Salmonson S. Sepke, B. Spears, P. T. Springer, C. A. Thomas, and R. Town, *in* preparation (2015).

[23]O. S. Jones, C. J. Cerjan, M. M. Marinak, J. L. Milovich, H. F. Robey, P. T. Springer, L. R. Benedetti, D. L. Bleuel, E. J. Bond, D. K. Bradley, D. A. Callahan, J. A. Caggiano, P. M. Celliers, D. S. Clark, S. M. Dixit, T. Döppner, R. J. Dylla-Spears, E. G. Dzentitis, D. R. Farley, S. M. Glenn, S. H. Glenzer, S. W. Haan, B. J. Haid, C. A. Haynam, D. G. Hicks, B. J. Kozioziemski, K. N. LaFortune, O. L. Landen, E. R. Mapoles, A. J. MacKinnon, J. M. McNaney, N. B. Meezan, P. A. Michel, J. D. Moody, M. J. Moran, D. H. Munro, M. V. Patel, T. G. Parham, J. D. Sater, S. M. Sepke, B. K. Spears, R. P. J. Town, S. V. Weber, K. Widmann, C. C. Widmayer, E. A. Williams, L. J. Atherton, M. J. Edwards, J. D. Lindl, B. J. MacGowan, L. J. Suter, R. E. Olson, H. W. Herrmann, J. L. Kline, G. A. Kyrala, D. C. Wilson, J. Frenje, T. R. Boehly, V. Glebov, J. P. Knauer, A. Nikroo, H. Wilkens, and J. D. Kilkenny, Phys. Plasmas **19**, 056315 (2012).

[24]J. A. Frenje, R. Bionta, E. J. Bond, J. A. Caggiano, D. T. Casey, C. Cerjan, J. Edwards, M. Eckart, D. N. Fittinghoff, S. Friedrich, V. Yu. Blebov, S. Blenzer, G. Grim, S. Haan, R. Hatarik, S. Hatchett, M. Gatu Johnson, O. S. Jones, J. D. Kilkenny, J. P. Knauer, O. Landen, R. Leeper, S. Le Pape, R. Lerche, C. K. Li, A. Mackinnon, J. McNaney, F. E. Merrill, M. Moran, D. H. Munro, T. J. Murphy, R. D. Petrasso, R. Rygg, T. C. Sangster, F. H. Séguin, S. Sepke, B. Spears, P. Springer, C. Stoeckl, and D. C. Wilson, Nuc. Fusion **53**, 043014 (2013).

[25]B. A. Hammel, R. Tommasini, D. S. Clark, J. Field, H. Robey, H. A. Scott, V. Smalyuk, M. Stadermann, C. Weber, in preparation (2015).

[26]J. R. Rygg, O. S. Jones, J. E. Field, M. A. Barrios, L. R. Benedetti, G. W. Collins, D. C. Eder, M. J. Edwards, J. L. Kline, J. J. Kroll, O. L. Landen, T. Ma, A. Pak, J. L. Peterson, K. Raman, R. P. J. Town, and D. K. Bradley, Phys. Rev. Lett. **112**, 195001 (2014).

[27]D. A. Callahan, O. A. Hurricane, D. E. Hinkel, T. Döppner, T. Ma, H.-S. Park, M. A. Barrios Garcia, L. F. Berzak Hopkins, D. T. Casey, C. J. Cerjan, E. L. Dewald, T. R. Dittrich, M. J. Edwards, S. W. Haan, A. V. Hamza, J. L. Kline, J. P. Knauer, A. L. Kritcher, O. L. Landen, S. LePape, A. G. MacPhee, J. L. Milovich, A. Nikroo, A. E. Pak, P. K. Patel, J. R. Rygg, J. E. Ralph, J. D. Salmonson, B. K. Spears, P. T. Springer, R. Tommasini, L. R. Benedetti, R. M. Bionta, E. J. Bond, D. K. Bradley, J. A. Caggiano, J. E. Field, D. N. Fitttinghoff, J. Frenje, M. Gatu Johnson, G. P. Grim, R. Hatarik, F. E. Merrill, S. R. Nagel, N. Izumi, S. F. Khan, R. P. J. Town, D. B. Sayer, P. Volegov, and C. H. Wilde, Phys. Plasmas **22**, 056314 (2015).

[28]H. F. Robey, T. R. Boehly, P. M. Celliers, J. H. Eggert, D. Hicks, R. F. Smith, R. Collins, M. W. Bowers, K. G. Krauter, P. S. Datte, D. H. Munro, J. L. Milovich, O. S. Jones, P. A. Michel, C. A. Thomas, R. E. Olson, S. Pollaine, R. P. J. Town, S. Haan, D. Callahan, D. Clark, J. Edwards, J. L. Kline, S. Dixit, M. B. Schneider, E. L. Dewald, K. Widmann, J. D. Moody, T. Döppner, H. B. Radousky, A. Throop, D. Kalantar, P. DiNicola, A. Nikroo, J. J. Kroll, A. V. Hamza, J. B. Horner, S. D. Bhandarkar, E. Dzenitis, E. Alger, E. Giraldez, C. Castro, K. Moreno, C. Haynam, K. N. LaFortune, C. Widmayer, M. Shaw, K. Jancaitis, T. Parham, D. M. Holunga, C. F. Walters, B. Haid, E. R. Mapoles, J. Sater, C. R. Gibson, T. Malsbury, J. Fair, D. Trummer, K. R. Coffee, B. Burr, L. V. Berzins, C. Choate, S. J. Brereton, S. Azevedo, H. Chandrasekaran, D. C. Eder, N. D. Masters, A. C. Fisher, P. A. Sterne, B. K. Young, O. L. Landen, B. M. Van Wonterghem, B. J. MacGowan, J. Atherton, J. D. Lindl, D. D. Meyerhofer, and E. Moses, Phys. Plasmas **19**, 042706 (2012).

[29]D. G. Hicks, N. B. Meezan, E. L. Dewald, A. J. Mackinnon, D. A. Callahan, T. Döppner, L. R. Benedetti, D. K. Bradley, P. M. Celliers, D. S. Clark, S. N. Dixit, E. G. Dzenitis, J. E. Eggert, D. R. Farley, S. M. Glenn, S. H. Glenzer, A. V. Hamza, R. F. Heeter, J. P. Holder, N. Izumi, D. H. Kalantar, S. F. Khan, J. J. Kroll, T. Ma, A. G. MacPhee, J. M. McNaney, J. D. Moody, M. J. Moran, B. R. Nathan, K. P. Opachich, R. R. Prasad, J. E. Ralph, H. F. Robey, J. R. Rygg, J. D. Salmonson, M. B. Schneider, N. Simanovskaia, B. K. Spears, R. Tommasini, K. Widmann, G. W. Collins, O. L. Landen, J. D. Kilkenny, W. W. Hsing, B. J. MacGowan, L. J. Atherton, M. J. Edwards, R. E. Olson, J. A Frenje, R. D. Petrasso, H. G. Rinderknecht, A. B. Zylstra, J. L Kline, G. A. Kyrala, and A. Nikroo, Phys. Plasmas **19**, 122702 (2012).

[30]S. A. MacLaren, M. B. Schneider, K. Widmann, J. H. Hammer, B. E. Yoxall, J. D. Moody, P. M. Bell, L. R. Benedetti, K. K. Bradley, and M. J. Edwards, Phys. Rev. Lett. **112**, 105003 (2014).

[31]H. Huang, R. B. Stephens, J. B. Gibson, and I. Valmainski, Fusion Sci. Technology **49**, 642 (2006).

[32]A. Q. L. Nguyen, S. A. Eddinger, H. Huang, M. A. Johnson, Y. T. Lee, R. C. Montesanti, K. A. Moreno, and M. E. Schoff, Fusion Sci. Technology **55**, 399 (2009).

[33]B. J. Kozioziemski, E. R. Mapoles, J. D. Sater, A. A. Chernov, J. D. Moody, J. B. Lugten, and M. A. Johnson, Fusion Sci. Technology **59**, 14 (2011).

[34]V. A. Smalyuk, M. Barrios, J. A. Caggiano, D. T. Casey, C. J. Cerjan, D. S. Clark, M. J. Edwards, J. A. Frenje, M. Gatu-Johnson, V. Y. Glebov, G. Grim, S. W. Haan, B. A. Hammel, A. Hamza, D. E. Hoover, W. W. Hsing, O. Hurricane, J. D. Kilkenny, J. L. Kline, J. P. Knauer, J. Kroll, O. L. Landen, J. D. Lindl, T. Ma, J. M. McNaney, M. Mintz, A. Moore, A. Nikroo, T. Parham, J. L. Peterson, R. Petrasso, L. Pickworth, J. E. Pino, K. Raman, S. P. Regan, B. A. Remington, H. F. Robey, D. P. Rowley, D. B. Sayre, R. E. Tipton, S. V. Weber, K. Widmann, D. C. Wilson, and C. B. Yeamans, Phys. Plasmas **21**, 056301 (2014).

[35]K. S. Raman, V. A. Smalyuk, D. T. Casey, S. W. Haan, D. E. Hoover, O. A. Hurricane, J. J. Kroll, A. Nikroo, J. L. Peterson, B. A. Remington, H. F. Robey, D. S. Clark, B. A. Hammel, O. L. Landen, M. M. Marinak, D. H. Munro, K. J. Peterson, and J. Salmonson, Phys. Plasmas **21**, 072710 (2014).

[36]D. T. Casey, V. A. Smalyuk, K. S. Raman, J. L. Peterson, L. Berzak Hopkins, D. A. Callahan, D. S. Clark, E. L. Dewald, T. R. Dittrich, S. W. Haan, D. E. Hinkel, D. Hoover, O. A. Hurricane, J. J. Kroll, O. L. Landen, A. S. Moore, A. Nikroo, H.-S. Park, B. A. Remington, H. F. Robey, J. R. Rygg, J. D. Salmonson, R. Tommasini, and K. Widmann, Phys. Rev. E **90**, 011102(R) (2014).

[37]C. R. Weber, D. S. Clark, A. W. Cook, L. E. Busby, and H. F. Robey, Phys. Rev. E **89**, 053106 (2014).

[38]C. R. Weber, D. S. Clark, A. W. Cook, D. C. Eder, S. W. Haan, B. A. Hammel, D. E. Hinkel, O. S. Jones, M. M. Marinak, J. L. Milovich, P. K. Patel, H. F. Robey, J. D. Salmonson, S. M. Sepke, and C. A. Thomas, Phys. Plasmas **22**, 032702 (2015).

[39]While Refs. 37, 38, and 13 showed that the hot spot flow fields are strongly modified due to viscous effects, including viscosity did not significantly impact the simulated observables (yield, DSR, ion temperature, etc.). Given the non-negligible increase in computational cost when viscosity is included, all of the simulations discussed in this paper were run without viscosity and accepted a small decrease in simulation fidelity for a significant savings in run time.

[40]G. P. Grim, N. Guler, F. E. Merrill, G. L. Morgan, C. R. Danly, P. L. Volegov, C. H. Wilde, D. C. Wilson, D. S. Clark, D. E. Hinkel, O. S. Jones, K. S. Raman, N. Izumi, D. N. Fittinghoff, O. B. Drury, E. T. Alger, P. A. Arnold, R. C. Ashabranner, L. J. Atherton, M. A. Barrios, S. Batha, P. M. Bell, L. R. Benedetti, R. L. Berger, L. A. Bernstein, L. V. Berzins, R. Betti, S. D. Bhandarkar, R. M. Bionta, D. L. Bleuel, T. R. Boehly, E. J. Bond, M. W. Bowers, D. K. Bradley, G. K. Brunton, R. A. Buckles, S. C. Burkhart, R. F. Burr, J. A. Caggiano, D. A. Callahan, D. T. Casey, C. Castro, P. M. Celliers, C. J. Cerjan, G. A. Chandler, C. Choate, S. J. Cohen, G. W. Collins, G. W. Cooper, J. R. Cox, J. R. Cradick, P. S. Datte, E. L. Dewald, P. Di Nicola, J. M. Di Nicola, L. Divol, S. N. Dixit, R. Dylla-Spears, E. G. Dzenitis, M. J. Eckart, D. C. Eder, D. H. Edgell, M. J. Edwards, J. H. Eggert, R. B. Ehrlich , G. V. Erbert, J. Fair, D. R. Farley, B. Felker, R. J. Fortner, J. A. Frenje, G. Frieders, S. Friedrich, M. Gatu-Johnson, C. R. Gibson, E. Giraldez, V. Y. Glebov, S. M. Glenn, S. H. Glenzer, G. Gururangan, S. W. Haan, K. D. Hahn, B. A. Hammel, A. V. Hamza, E. P. Hartouni, R. Hatarik, S. P. Hatchett, C. Haynam, M. R. Hermann, H. W. Herrmann, D. G. Hicks, J. P. Holder, D. M. Holunga, J. B. Horner, W. W. Hsing, H. Huang, M. C. Jackson , K. S. Jancaitis, D. H. Kalantar, R. L. Kauffman, M. I. Kauffman, S. F. Khan, J. D. Kilkenny, J. R. Kimbrough, R. Kirkwood, J. L. Kline, J. P. Knauer, K. M. Knittel, J. A. Koch, T. R. Kohut, B. J. Kozioziemski, K. Krauter, G. W. Krauter, A. L. Kritcher, J. Kroll, G. A. Kyrala, K. N. La Fortune, G. LaCaille, L. J. Lagin, T. A. Land, O. L. Landen, D. W. Larson, D. A. Latray, R. J. Leeper, T. L. Lewis, S. LePape, J. D. Lindl, R. R. Lowe-Webb, T. Ma, B. J. MacGowan, A. J. MacKinnon, A. G. MacPhee, R. M. Malone, T. N. Malsbury, E. Mapoles, C. D. Marshall, D. G. Mathisen, P. McKenty, J. M. McNaney, N. B. Meezan, P. Michel, J. L. Milovich, J. D. Moody, A. S. Moore, M. J. Moran, K. Moreno, E. I. Moses, D. H. Munro, B. R. Nathan, A. J. Nelson, A. Nikroo, R. E. Olson, C. Orth, A. E. Pak, E. S. Palma, T. G. Parham, P. K. Patel, R. W. Patterson, R. D. Petrasso, R. Prasad, J. E. Ralph, S. P. Regan, H. Rinderknecht, H. F. Robey, G. F. Ross, C. L. Ruiz, F. H. Séguin, J. D. Salmonson, T. C. Sangster, J. D. Sater, R. L. Saunders, M. B. Schneider, D. H. Schneider, M. J. Shaw, N. Simanovskaia, B. K. Spears, P. T. Springer, C. Stoeckl, W. Stoeffl, L. J. Suter, C. A. Thomas, R. Tommasini, R. P. Town, A. J. Traille, B. Van Wonterghem, R. J. Wallace, S. Weaver, S. V. Weber, P. J. Wegner, P. K. Whitman, K. Widmann, C. C. Widmayer, R. D. Wood, B. K. Young, R. A. Zacharias, and A. Zylstra, Phys. Plasmas **20**, 056320 (2013).

[41]There is similarly no inter-material diffusivity capability currently available in HYDRA.

[42]D. S. Clark, J. L. Milovich, D. E. Hinkel, J. D. Salmonson, J. L. Peterson, L. F. Berzak Hopkins, D. C. Eder, S. W. Haan, O. S. Jones, M. M. Marinak, H. F. Robey, V. A. Smalyuk, and C. R. Weber, Phys. Plasmas **21**, 112705 (2014).

[43]K. L. Baker, H. F. Robey, J. L. Milovich, O. S. Jones, V. A. Smalyuk, D. T. Casey, A. G. MacPhee, A. Pak, P. M. Celliers, D. S. Clark, O. L. Landen, J. L. Peterson, L. F. Berzak-Hopkins, C. R. Weber, S. W. Haan, T. D. Döppner, S. Dixit, E. Graldez, A. V. Hamza, K. S. Jancaitis, J. J. Kroll, K. N. Lafortune, B. J. MacGowna, J. D. Moody, A. Nikroo, and C. C. Widmayer, Phys. Plasmas **22**, 052702 (2015).

[44]A. G. MacPhee, J. L. Peterson, D. T. Casey, D. S. Clark, S. W. Haan, O. S. Jones, O. L. Landen, J. L. Milovich, H. F. Robey, and V. A. Smalyuk, Phys. Plasmas **22**, 080702 (2015).

[45]D. Casey, J. Milovich, V. Smalyuk, D. Clark, H. Robey, A. Pak, A. MacPhee, K. Baker, T. Ma, H.-S. Park, T. Döppner, D. Callahan, S. Haan, L. Peterson, P. Patel, A. Hamza, O. Jones, C. Weber, D. Hoover, A. Nikroo, C. Yeamans, F. Merrill, P. L. Volegov, D. Fittinghoff, G. Grim, S. Nagel, R. Benedetti, N. Izumi, J. Edwards, S. Khan, D. Sayre, R. Hatarik, E. Bond, C. Cerjan, M. Gatu Johnson, J. Frenje, and D. Edgell, Phys. Rev. Lett. **115**, 105001 (2015).

[46]J. Milovich, H. F. Robey, D. S. Clark, K. L. Baker, D. A. Callahan, D. T. Casey, C. Cerjan, A. G. MacPhee, A. Pak, P. K. Patel, J. L. Peterson, V. A. Smalyuk, and C. R. Weber, Phys. Plasmas, *to appear* (2015).

[47]M. Gatu Johnson, J. A. Frenje, D. T. Casey, C. K. Li, F. H. Séguin, R. Petrasso, R. Ashabranner, R. M. Bionta, D. L. Bleuel, E. J. Bond, J. A. Caggiano, A. Carpenter, C. J. Cerjan, T. J. Clancy, T. Doeppner, M. J. Eckart, M. J. Edwards, S. Friedrich, S. H. Glenzer, S. W. Haan, E. P. Hartouni, R. Hatarik, S. P. Hatchett, O. S. Jones, G. Kyrala, S. Le Pape, R. A Lerche, O. L. Landen, T. Ma, A. J. MacKinnon, M. A. McKernan, M. J. Moran, E. Moses, D. H. Munro, J. McNaney, H. S. Park, J. Ralph, B. Remington, J. R. Rygg, S. M. Sepke, V. Smalyuk, B. Spears, P. T. Springer, C. B. Yeamans, M. Farrell, D. Jasion, J. D. Kilkenny, A. Nikroo, R. Paguio, J. P. Knauer, V. Yu Glebov, T. C. Sangster, R. Betti, C. Stoeckl, J. Magoon, M. J. Shoup III, G. P. Grim, J. Kline, G. L. Morgan, T. J. Murphy, R. J. Leeper, C. L. Ruiz, G. W. Cooper, and A. J. Nelson, Rev. Sci. Instrum. **83**, 10D308 (2012).

[48]B. A. Hammel, S. W. Haan, D. S. Clark, M. J. Edwards, S. H. Langer, M. M. Marinak, M. V. Patel, J. D. Salmonson, and H. A. Scott, High Energy Density Physics **6**, 171 (2010).

[49]D. S. Clark, S. W. Haan, A. W. Cook, M. J. Edwards, B. A. Hammel, J. M. Koning, and M. M. Marinak, Phys. Plasmas **18**, 082701 (2011).

[50]T. Döppner, C. A. Thomas, L. Divol, E. L. Dewald, P. M. Celliers, D. K. Bradley, D. A. Callahan, S. N. Dixit, J. A. Harte, S. M. Glenn, S. W. Haan, N. Izumi, G. A. Kyrala, G. LaCaille, J. K. Kline, W. L. Kruer, T. Ma, A. J. MacKinnon, J. M. McNaney, N. B. Meezan, H. F. Robey, J. D. Salmonson, L. J. Suter, G. B. Zimmerman, M. J. Edwards, B. J. MacGownan, J. D. Kilkenny, J. D. Lindl, B. M. Van Wonterghem, L. J. Atherton, E. I. Moses, S. H. Glenzer, and O. L. Landen, Phys. Rev. Lett. **108**, 135006 (2012).

[51]H. F. Robey, V. A. Smalyuk, J. L. Milovich, T. Döppner, D. T. Casey, K. L. Baker, J. L. Peterson, B. Bachmann, L. F. Berzak Hopkins, E. Bond, J. A. Caggiano, D. A. Callahan, P. M. Celliers, C. Cerjan, D. S. Clark, S. N. Dixit, M. J. Edwards, N. Gharibyan, S. W. Haan, B. A. Hammel, A. V. Hamza, R. Hatarik, O. A. Hurricane, K. S. Jancaitis, O. S. Jones, G. D. Kerbel, J. J. Kroll, K. N. Lafortune, O. L. Landen, T. Ma, M. M. Marinak, B. J. MacGowna, A. G. MacPhee, A. Pak, M. Patel, P. K. Patel, L. J. Perkins, D. B. Sayre, S. M. Sepke, B. K. Spears, R. Tommasini, C. R. Weber, C. C. widmayer, C. Yeamans, E. Giraldez, D. Hoover, A. Nikroo, M. Hohenberger, and M. Gatu Johnson, Phys. Plasmas, *submitted* (2015).

[52]L. Kelvin, Philos. Mag. **42**, 362 (1871).

[53]H. von Helmholtz, Mon. Rep. R. Prussian Acad. Philos. Berlin **23**, 215 (1868).

[54]G. A. Kyrala, J. L. Kline, S. Dixit, S. Glenzer, D. Kalantar, D. Badley, N. Izumi, N. Meezan, O. Landen, D. Callahan, S. V. Weber, J. P. Holder, S. Glenn, M. J. Edwards, J. Koch, L. J. Suter, S. W. Haan, R. P. J. Town, P. Michel, O. Jones, S. Langer, J. D. Moody, E. L. Dewald, T. Ma, J. Ralph, A. Hamza, E. Dzenitis, and J. Kilkenny, Phys. Plasmas **18**, 056307 (2011).

[55]S. H. Glenzer, D. A. Callahan, A. J. MacKinnon, J. L. Kline, G. Grim, E. T. Alger, R. L. Berger, L. A. Bernstein, R. Betti, D. L. Bleuel, T. R. Boehly, D. K. Bradley, S. C. Burkhart, R. Burr, J. A. Caggiano, C. Castro, D. T. Casey, C. Choate, D. S. Clark, P. Celliers, C. J. Cerjan, G. W. Collins, E. L. Dewald, P. DiNicola, J. M. DiNicola, L. Divol, S. Dixit, T. Döppner, R. Dylla-Spears, E. Dzenitis, M. Eckart, G. Erbert, D. Farley, J. Fair, D. Fittinghoff, M. Frank, L. J. A. Frenje, S. Friedrich, D. T. Casey, M. Gatu Johnson, C. Gibson, E. Giraldez, V. Glebov, S. Glenn, N. Guler, S. W. Haan, B. J. Haid, B. A. Hammel, A. V. Hamza, C. A. Haynam, G. M. Heestand, M. Hermann, H. W. Hermann, D. G. Hicks, D. E. Hinkel, J. P. Holder, D. M. Holunda, J. B. Horner, W. W. Hsing, H. Huang, N. Izumi, M. Jackson, O. S. Jones, D. H. Kalantar, R. Kauffman, J. D.

Kilkenny, R. K. Kirkwood, J. Klingmann, T. Kohut, J. P. Knauer, J. A. Koch, B. Kozioziemki, G. A. Kyrala, A. L. Kritcher, J. Kroll, K. La Fortune, L. Lagin, O. L. Landen, D. W. Larson, D. LaTray, R. J. Leeper, S. Le Pape, J. D. Lindl, R. Lowe-Webb, T. Ma, J. McNaney, A. G. MacPhee, T. N. Malsbury, E. Mapoles, C. D. Marshall, N. B. Meezan, F. Merrill, P. Michel, J. D. Moody, A. S. Moore, M. Moran, K. A. Moreno, D. H. Munro, B. R. Nathan, A. Nikroo, R. E. Olson, C. D. Orth, A. E. Pak, P. K. Patel, T. Parham, R. Petrasso, J. E. Ralph, H. Rinderknecht, S. P. Regan, H. F. Robey, J. S. Ross, M. D. Rosen, R. Sacks, J. D. Salmonson, R. Saunders, J. Sater, C. Sangster, M. B. Schneider, F. H. Séguin, M. J. Shaw, B. K. Spears, P. T. Springer, W. Stoeffl, L. J. Suter, C. A. Thomas, R. Tommasini, R. P. J. Town, C. Walters, S. Weaver, S. V. Weber, P. J. Wegner, P. K. Whitman, K. Widmann, C. C. Widmayer, C. H. Wilde, D. C. Wilson, B. Van Wonterghem, B. J. MacGowan, L. J. Atherton, M. J. Edwards and E. I. Moses, Phys. Plasmas **19**, 056318 (2012).

[56]R. P. J. Town, D. K. Bradley, A. Kritcher, O. S. Jones, J. R. Rygg, R. Tommasini, M. Barrios, L. R. Benedetti, L. F. Berzak Hopkins, P. M. Celliers, T. Döppner, E. L. Dewald, D. C. Eder, J. E. Field, S. M. Glenn, N. Izumi, S. W. Haan, S. F. Khan, J. L. Kline, G. A. Kyrala, T. Ma, J. L. Milovich, J. D. Moody, S. R. Nagel, A. Pak, J. L. Peterson, H. F. Robey, J. S. Ross, R. H. H. Scott, B. K. Spears, M. J. Edwards, J. D. Kilkenny, and O. L. Landen, Phys. Plasmas **21**, 056313 (2014).

[57]S. M. Pollaine, Nuc. Fusion **40**, 2061 (2000).

[58]O. S. Jones, N. Izumi, S. R. Nagel, P. A. Amendt, G. N. Hall, L. Berzak Hopkins, S. F. Khan, A. S. Moore, J. E. Ralph, J. R. Rygg, M. B. Schneider, D. J. Strozzi, D. P. Turnbull, and K. Widmann, Phys. Rev. Lett., *submitted* (2015).